Comparing Post-Newtonian and Numerical-Relativity Precession Dynamics

Serguei Ossokine,[1,2] Michael Boyle,[3] Lawrence E. Kidder,[3] Harald P. Pfeiffer,[1,4] Mark A. Scheel,[5] and Béla Szilágyi[5]

[1] *Canadian Institute for Theoretical Astrophysics, University of Toronto, Toronto, Ontario M5S 3H8, Canada*
[2] *Department of Astronomy and Astrophysics, 50 St. George Street, University of Toronto, Toronto, ON M5S 3H4, Canada*
[3] *Center for Radiophysics and Space Research, Cornell University, Ithaca, New York, 14853*
[4] *Canadian Institute for Advanced Research, 180 Dundas St. West, Toronto, ON M5G 1Z8, Canada*
[5] *Theoretical Astrophysics 350-17, California Institute of Technology, Pasadena, CA 91125*

(Dated: February 9, 2015)

Binary black-hole systems are expected to be important sources of gravitational waves for upcoming gravitational-wave detectors. If the spins are not colinear with each other or with the orbital angular momentum, these systems exhibit complicated precession dynamics that are imprinted on the gravitational waveform. We develop a new procedure to match the precession dynamics computed by post-Newtonian (PN) theory to those of numerical binary black-hole simulations in full general relativity. For numerical relativity (NR) simulations lasting approximately two precession cycles, we find that the PN and NR predictions for the directions of the orbital angular momentum and the spins agree to better than $\sim 1^\circ$ with NR during the inspiral, increasing to 5° near merger. Nutation of the orbital plane on the orbital time-scale agrees well between NR and PN, whereas nutation of the spin direction shows qualitatively different behavior in PN and NR. We also examine how the PN equations for precession and orbital-phase evolution converge with PN order, and we quantify the impact of various choices for handling partially known PN terms.

I. INTRODUCTION

Binary black holes (BBH) are among the most important sources of gravitational waves for upcoming gravitational-wave detectors like Advanced LIGO [1] and Virgo [2]. Accurate predictions of the gravitational waveforms emitted by such systems are important for detection of gravitational waves and for parameter estimation of any detected binary [3]. When either black hole carries spin that is *not* aligned with the orbital angular momentum, there is an exchange of angular momentum between the components of the system, leading to complicated dynamical behavior. Figure 1 exhibits the directions of the various angular momenta in several simulations described in this paper. This behavior is imprinted on the emitted waveforms [4–6], making them more feature-rich than waveforms from aligned-spin BBH systems or non-spinning BBH systems. In order to model the waveforms accurately, then, we need to understand the dynamics.

The orbital-phase evolution of an inspiraling binary, the precession of the orbital angular momentum and the black-hole spins, and the emitted gravitational waveforms can be modeled with post-Newtonian theory [7], a perturbative solution of Einstein's equations in powers of v/c, the ratio of the velocity of the black holes to the speed of light. Such post-Newtonian waveforms play an important role in the waveform modeling for ground-based interferometric gravitational-wave detectors (see, e.g., [8]). For non-spinning and aligned-spin BBH, however, the loss of accuracy of the post-Newtonian phase evolution in the late inspiral has been identified as one of the dominant limitations of waveform modeling [9–14].

Precessing waveform models (e.g., [6, 15–17]) depend on the orbital phase evolution and the precession dynamics. Therefore, it is important to quantify the accuracy of the post-Newtonian approximation for modeling the precession dynamics itself, and the orbital-phase evolution of precessing binaries. Recently, the SXS collaboration has published numerical-relativity solutions to the full Einstein equations for precessing BBH systems [18]. These simulations cover $\gtrsim 30$ orbits and up to two precession cycles. Therefore, they offer a novel opportunity to systematically quantify the accuracy of the post-Newtonian precession equations, the topic of this paper.

In this paper, we develop a new technique to match the initial conditions of post-Newtonian dynamics to a numerical relativity simulation. We then use this technique to study the level of agreement between the post-Newtonian precession equations and the numerical simulations. The agreement is remarkably good, the directions of orbital angular momentum and spin axes in post-Newtonian theory reproduces the numerical simulations usually to better than 1 degree. We also investigate nutation effects on the orbital time-scale that are imprinted both in the orbital angular momentum and the spin-directions. For the orbital angular momentum, NR and PN yield very similar nutation features, whereas for the spin direction, nutation is qualitatively different in PN and the investigated NR simulations. Considering the orbital-phase evolution, we find that the disagreement between post-Newtonian orbital phase and numerical relativity simulation is comparable to the aligned-spin case. This implies that the orbital phase evolution will remain an important limitation for post-Newtonian waveforms even in the precessing case. Finally, we study the convergence with post-Newtonian order of the precession equations, and establish very regular and fast convergence, in contrast to post-Newtonian orbital phasing.

This paper is organized as follows: Section II describes the post-Newtonian expressions utilized, the numerical simulations, how we compare PN and NR systems with each other, and how we determine suitable "best-fitting"

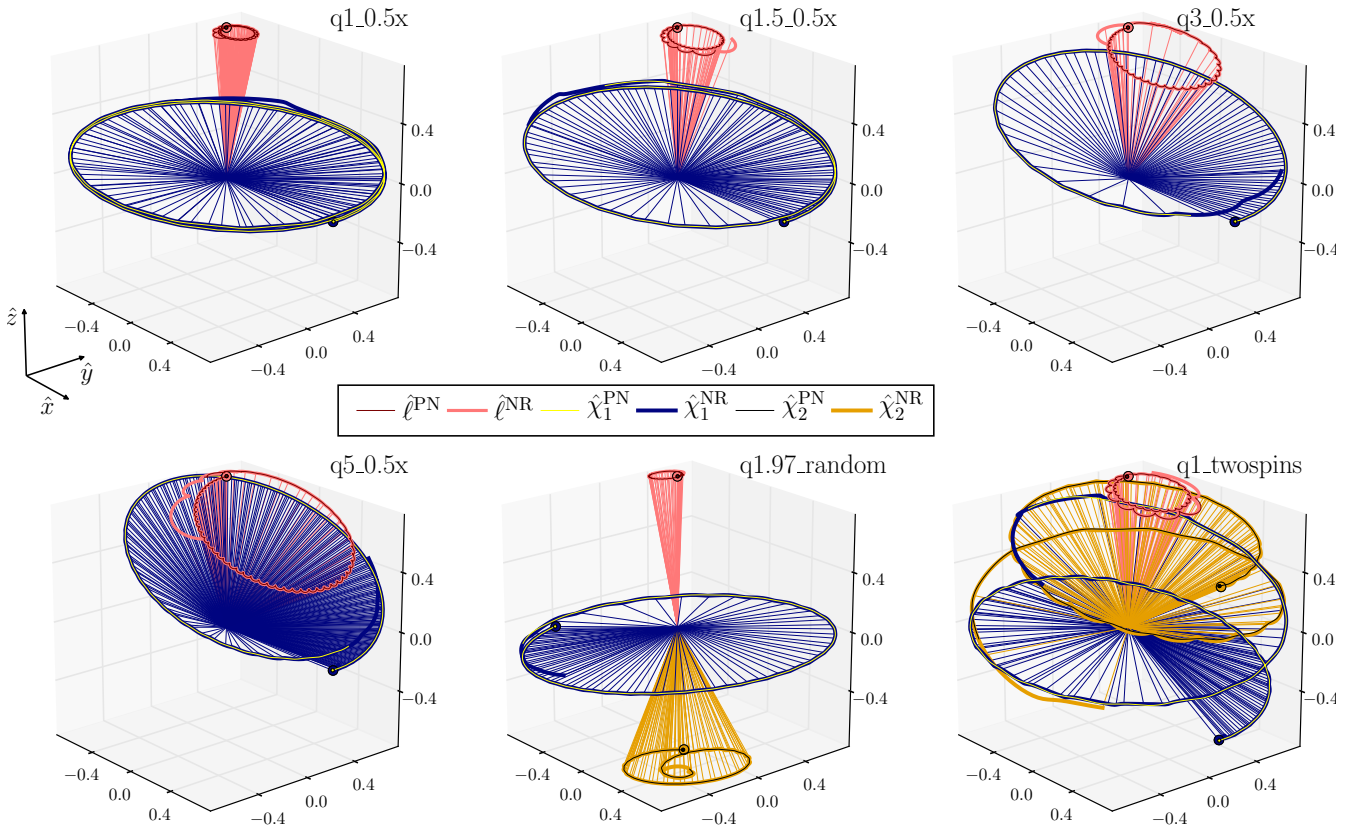

FIG. 1. Precession cones of the six primary precessing simulations considered here, as computed by NR and PN. Shown are the paths traced on the unit sphere by the normal to the orbital plane $\hat{\ell}$ and the spin-directions $\hat{\chi}_{1,2}$. The thick lines represent the NR data, with the filled circles indicating the start of the NR simulations. The lines connecting the NR data to the origin are drawn to help visualize the precession-cones. The PN data, plotted with thin lines, lie on the scale of this figure almost precisely on top of the NR data. (The PN data was constructed using the Taylor T4 approximant matched at frequency $m\Omega_m = 0.021067$, with a matching interval width $\delta\Omega = 0.1\Omega_m$.)

PN parameters for a comparison with a given NR simulation. Section III presents our results, starting with a comparison of the precession dynamics in Sec. III A, and continuing with an investigation in the accuracy of the orbital phasing in Sec. III B. The following two sections study the convergence of the PN precession equations and the impact of ambiguous choices when dealing with incompletely known spin-terms in the PN orbital phasing. Section III E, finally, is devoted to some technical numerical aspects, including an investigation into the importance of the gauge conditions used for the NR runs. We close with a discussion in Sec. IV. The appendices collect the precise post-Newtonian expressions we use and additional useful formulae about quaternions.

II. METHODOLOGY

A. Post-Newtonian Theory

Post-Newtonian (PN) theory is an approximation to General Relativity in the weak-field, slow-motion regime, characterized by the small parameter $\epsilon \sim (v/c)^2 \sim \frac{Gm}{rc^2}$, where m, v, and r denote the characteristic mass, velocity, and size of the source, c is the speed of light, and G is Newton's gravitational constant. For the rest of this paper, the source is always a binary black-hole system with total mass m, relative velocity v and separation r, and we use units where $G = c = 1$.

Restricting attention to quasi-spherical binaries in the adiabatic limit, the local dynamics of the source can be split into two parts: the evolution of the orbital frequency, and the precession of the orbital plane and the spins. The leading-order precessional effects [19] and spin contributions to the evolution of the orbital frequency [20, 21] enter post-Newtonian dynamics at the 1.5 PN order (i.e., $\epsilon^{3/2}$) for spin-orbit effects, and 2 PN order for spin-spin effects. We also include non-spin terms to 3.5 PN order [7], the spin-orbit terms to 4 PN order [22], spin-spin terms to 2 PN order [21][1]. For the precession equations, we include the spin-orbit contribu-

[1] During the preparation of this manuscript, the 3 PN spin-spin contributions to the flux and binding energy were completed in [23]. These terms are not used in the analysis presented here.

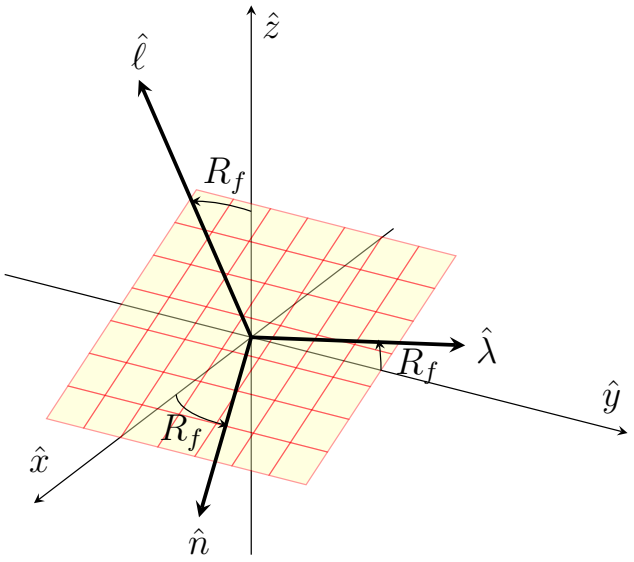

FIG. 2. Vectors describing the orbital dynamics of the system. The yellow plane denotes the orbital plane. $R_{\rm f}(t)$ is the rotor that rotates the coordinate triad $(\hat{x}, \hat{y}, \hat{z})$ into the orbital triad $(\hat{n}, \hat{\lambda}, \hat{\ell})$.

tions to next-to-next-to-leading order, corresponding to 3.5 PN [24]. The spin-spin terms are included at 2 PN order[2].

1. *Orbital dynamics*

Following earlier work (e.g., Ref. [21]) we describe the precessing BH binary by the evolution of the orthonormal triad $(\hat{n}, \hat{\lambda}, \hat{\ell})$, as indicated in Fig. 2: $\hat{n}$ denotes the unit separation vector between the two compact objects, $\hat{\ell}$ is the normal to the orbital plane and $\hat{\lambda} = \hat{\ell} \times \hat{n}$ completes the triad. This triad is time-dependent, and is related to the constant inertial triad $(\hat{x}, \hat{y}, \hat{z})$ by a time-dependent rotation R_f, as indicated in Fig. 2. The rotation R_f will play an important role in Sec. II C. The orbital triad obeys the following equations:

$$\frac{d\hat{\ell}}{dt} = \varpi \hat{n} \times \hat{\ell}, \tag{1a}$$

$$\frac{d\hat{n}}{dt} = \Omega \hat{\lambda}, \tag{1b}$$

$$\frac{d\hat{\lambda}}{dt} = -\Omega \hat{n} + \varpi \hat{\ell}. \tag{1c}$$

Here, Ω is the instantaneous orbital frequency and ϖ is the precession frequency of the orbital plane.

The dimensionless spin vectors $\vec{\chi}_i = \vec{S}_i/m_i^2$ also obey precession equations:

$$\frac{d\vec{\chi}_1}{dt} = \vec{\Omega}_1 \times \vec{\chi}_1, \tag{2a}$$

$$\frac{d\vec{\chi}_2}{dt} = \vec{\Omega}_2 \times \vec{\chi}_2. \tag{2b}$$

The precession frequencies $\vec{\Omega}_{1,2}$, ϖ are series in the PN expansion parameter ϵ; their explicit form is given in Appendix A.

The evolution of the orbital frequency is derived from energy balance:

$$\frac{dE}{dt} = -\mathcal{F}, \tag{3}$$

where E is the energy of the binary and $\mathcal{F}$ is the gravitational-wave flux. E and $\mathcal{F}$ are PN series depending on the orbital frequency Ω, the vector $\hat{\ell}$, and the BH spins $\vec{\chi}_1$, $\vec{\chi}_2$. Their explicit formulas are given in Appendix A. In terms of $x \equiv (m\Omega)^{2/3} \sim \epsilon$, Eq. (3) becomes:

$$\frac{dx}{dt} = -\frac{\mathcal{F}}{dE/dx}, \tag{4}$$

where the right-hand side is a ratio of two PN series.

There are several well known ways of solving Eq. (4), which lead to different treatment of uncontrolled higher-order PN terms—referred to as the Taylor T1 through T5 approximants [30, 31]. The T2 and T3 approximants cannot be applied to general precessing systems; we therefore exclude them from this work. We now briefly review the remaining approximants, which will be used throughout this work.[3] The most straightforward approach is to evaluate the numerator and denominator of Eq. (4) and then solve the resulting ordinary differential equation numerically, which is the Taylor T1 approximant. Another approach is to re-expand the ratio $\mathcal{F}/(dE/dx)$ in a new power series in x, and then truncate at the appropriate order. This gives the Taylor T4 approximant. Finally, one can expand the *inverse of the right-hand-side of Eq.* (4) in a new power series in x, truncate it at the appropriate order, and then substitute the inverse of the truncated series into the right-hand side in Eq. (4). This last approach, known as the Taylor T5 approximant [31], has been introduced fairly recently.

2. *Handling of spin terms*

When constructing Taylor approximants that include the re-expansion of the energy balance equation, the handling of spin terms becomes important. In particular,

[2] The investigation of the effects of spin-spin terms at higher PN orders (see e.g. [25–27] and references therein), and terms which are higher order in spin (e.g cubic spin terms) [28, 29] is left for future work.

[3] See, e.g., Ref. [32] for a more complete description of approximants T1 through T4.

TABLE I. Numerical relativity simulations utilized here. SXS ID refers to the simulation number in Ref. [18], $q = m_1/m_2$ is the mass ratio, $\vec{\chi}_{1,2}$ are the dimensionless spins, given in coordinates where $\hat{n}(t=0) = \hat{x}$, $\hat{\ell}(t=0) = \hat{z}$. D_0, Ω_0 and e are the initial coordinate separation, the initial orbital frequency, and the orbital eccentricity, respectively. The first block lists the precessing runs utilized, where $\vec{\chi}_{1,r} = (-0.18, -0.0479, -0.0378)$ and $\vec{\chi}_{2,r} = (-0.0675, 0.0779, -0.357)$. The second block indicates 31 further precessing simulations used in Fig. 10, and the last block lists the aligned spin systems for orbital phase comparisons.

Name	SXS ID	q	$\vec{\chi}_1$	$\vec{\chi}_2$	D_0/M	$m\Omega_0$	e
q1_0.5x	0003	1.0	(0.5,0.0,0)	(0,0,0)	19	0.01128	0.003
q1.5_0.5x	0017	1.5	(0.5,0,0)	(0,0,0)	16	0.01443	$< 2 \times 10^{-4}$
q3_0.5x	0034	3.0	(0.5,0,0)	(0,0,0)	14	0.01743	$< 2 \times 10^{-4}$
q5_0.5x		5.0	(0.5,0,0)	(0,0,0)	15	0.01579	0.002
q1_two_spins	0163	1.0	(0.52,0,-0.3)	(0.52,0,0.3)	15.3	0.01510	0.003
q1.97_random	0146	1.97	$\vec{\chi}_{1,r}$	$\vec{\chi}_{2,r}$	15	0.01585	$< 10^{-4}$
31 random runs	115–145	$[1, 2]$	$\chi_1 \leq 0.5$	$\chi_2 \leq 0.5$	15	≈ 0.0159	$[10^{-4}, 10^{-3}]$
q1_0.5z	0005	1.0	(0,0,0.5)	(0,0,0)	19	0.01217	0.0003
q1_-0.5z	0004	1.0	(0,0,0.5)	(0,0,0)	19	0.01131	0.0004
q1.5_0.5z	0013	1.5	(0,0,0.5)	(0,0,0)	16	0.01438	0.00014
q1.5_-0.5z	0012	1.5	(0,0,-0.5)	(0,0,0)	16	0.01449	0.00007
q3_0.5z	0031	3.0	(0,0,0.5)	(0,0,0)	14	0.01734	$< 10^{-4}$
q3_-0.5z	0038	3.0	(0,0,-0.5)	(0,0,0)	14	0.01756	$< 10^{-4}$
q5_0.5z	0061	5.0	(0,0,0.5)	(0,0,0)	15	0.01570	0.004
q5_-0.5z	0060	5.0	(0,0,-0.5)	(0,0,0)	15	0.01591	0.003
q8_0.5z	0065	8.0	(0,0,0.5)	(0,0,0)	13	0.01922	0.004
q8_-0.5z	0064	8.0	(0,0,-0.5)	(0,0,0)	13	0.01954	0.0005

terms of quadratic and higher order in spins, such as $(\vec{S}_i)^2$, appear in the evolution of the orbital frequency at 3 PN and higher orders. These terms arise from lower-order effects and represent incomplete information, since the corresponding terms are unknown in the original power series for the binding energy E and the flux $\mathcal{F}$,

$$E(x) = -\frac{1}{2} m\nu x \left(1 + \sum_{k=2} a_k x^{k/2}\right), \tag{5}$$

$$\mathcal{F}(x) = \frac{32}{5}\nu^2 x^5 \left(1 + \sum_{k=2} b_k x^{k/2}\right), \tag{6}$$

where $m = m_1 + m_2$ and $\nu = m_1 m_2/m^2$, and $m_{1,2}$ are the individual masses.

In these expansions, the spin-squared terms come in at 2 PN order and thus appear in a_4 and b_4, cf. Eqs. (A18) and (A24). Then, in the re-expansion series of Taylor T4,

$$S \equiv -\frac{\mathcal{F}}{dE/dx} = \frac{64\nu}{5m} x^5 (1 + \sum_{k=2} s_k x^{k/2}), \tag{7}$$

the coefficients s_k can be recursively determined, e.g.

$$s_4 = b_4 - 3a_4 - 2s_2 a_2, \tag{8}$$

$$s_6 = b_6 - (4a_6 + 3s_2 a_4 + \frac{5}{2} s_3 a_3 + 2s_4 a_2). \tag{9}$$

Thus, the spin-squared terms in a_4 and b_4 will induce spin-squared terms at 3PN order in s_6. The analogous conclusion holds for Taylor T5. These spin-squared terms are incomplete as the corresponding terms in the binding energy and flux (i.e. in a_6 and b_6) are not known.

This re-expansion has been handled in several ways in the literature. For example, Nitz et al. [14] include only terms which are linear in spin beyond 2 PN order. On the other hand, Santamaría et al. [33] keep *all* terms in spin arising from known terms in E and $\mathcal{F}$. In the present work, we also keep all terms up to 3.5 PN order, which is the highest order to which non-spin terms are completely known. Similarly, we include all terms when computing the precession frequency (see A 2). We investigate the impact of different spin-truncation choices in Sec. III D, along with the impact of partially known 4 PN spin terms.

B. Numerical Relativity Simulations

To characterize the effectiveness of PN theory in reproducing NR results, we have selected a subset of 16 simulations from the SXS waveform catalog described in Ref. [18].[4] Our primary results are based on six precessing simulations and a further ten non-precessing ones for cross-comparisons. To check for systematic effects, we use a further 31 precessing simulations with random mass-ratios and spins. The parameters of these runs are

[4] The waveform and orbital data are publicly available at https://www.black-holes.org/waveforms/.

given in Table I. They were chosen to represent various degrees of complexity in the dynamics: (i) precessing versus non-precessing simulations, the latter with spins parallel or anti-parallel to $\hat{\ell}$; (ii) one versus two spinning black holes; (iii) coverage of mass ratio from $q = 1$ to $q = 8$; (iv) long simulations that cover more than a precession cycle; and (v) a variety of orientations of $\hat{\chi}_1, \hat{\chi}_2, \hat{\ell}$. Figure 1 shows the precession cones of the normal to the orbital plane and the spins for for the six primary precessing cases in Table I. The PN data were computed using the Taylor T4 3.5 PN approximant.

The simulations from the catalog listed in Table I were run with numerical methods similar to [34]. A generalized harmonic evolution system [35–38] is employed, and the gauge is determined by gauge source functions H_a. During the inspiral phase of the simulations considered here, H_a is kept constant in the co-moving frame, cf. [32, 39, 40]. About 1.5 orbits before merger, the gauge is changed to damped harmonic gauge [41–43]. This gauge change happens outside the focus of the comparisons presented here.

The simulation q5_0.5x analyzed here is a re-run of the SXS simulation SXS:BBH:0058 from Ref. [18]. We performed this re-run for two reasons: First, SXS:BBH:0058 changes to damped harmonic gauge in the middle of the inspiral, rather than close to merger as all other cases considered in this work. Second, SXS:BBH:0058 uses an unsatisfactorily low numerical resolution during the calculation of the black hole spins. Both these choices leave noticeable imprints on the data from SXS:BBH:0058, and the re-run q5_0.5x allows us to quantify the impact of these deficiencies. We discuss these effects in detail in Secs. III E 2 and III E 3. The re-run q5_0.5x analyzed here is performed with improved numerical techniques. Most importantly, damped harmonic gauge is used essentially from the start of the simulation, $t \gtrsim 100M$. The simulation q5_0.5x also benefits from improved adaptive mesh refinement [44] and improved methods for controlling the shape and size of the excision boundaries; the latter methods are described in Sec.II.B. of Ref. [45].

We have performed convergence tests for some of the simulations; Sec. III E will demonstrate with Fig. 16 that numerical truncation error is unimportant for the comparisons presented here.

C. Characterizing Precession

The symmetries of non-precessing systems greatly simplify the problem of understanding the motion of the binary. In a non-precessing system, the spin vectors are essentially constant, and two of the rotational degrees of freedom are eliminated in the binary's orbital elements. Assuming quasi-circular orbits, the entire system can be described by the orbital phase Φ, which can be defined as the angle between $\hat{n}$ and $\hat{x}$. In post-Newtonian theory the separation between the black holes can be derived from $d\Phi/dt$. Thus comparison between post-Newtonian and numerical orbits, for example, reduces entirely to the comparison between $\Phi_{\rm PN}$ and $\Phi_{\rm NR}$ [32, 46]. For precessing systems, on the other hand, the concept of an orbital phase is insufficient; Φ could be thought of as just one of the three Euler angles. We saw in Sec. II A 1 that the orbital dynamics of a precessing system can be fairly complex, involving the triad $(\hat{n}, \hat{\lambda}, \hat{\ell})$ (or equivalently the frame rotor $R_{\rm f}$) as well as the two spin vectors $\vec{\chi}_1$ and $\vec{\chi}_2$—each of which is, of course, time dependent. When comparing post-Newtonian and numerical results, we need to measure differences between each of these quantities in their respective systems.

To compare the positions and velocities of the black holes themselves, we can condense the information about the triads into the quaternion quantity [47]

$$R_\Delta := R_{\rm f}^{\rm PN}\, \bar{R}_{\rm f}^{\rm NR}\ , \tag{10}$$

which represents the rotation needed to align the PN frame with the NR frame. This is a geometrically meaningful measure of the relative difference between two frames. We can reduce this to a single real number by taking the magnitude of the logarithm of this quantity, defining the angle[5]

$$\Phi_\Delta := 2\,|\log R_\Delta|\ . \tag{11}$$

This measure has various useful qualities. It is invariant, in the sense that any basis frame used to define $R_{\rm f}^{\rm PN}$ and $R_{\rm f}^{\rm NR}$ will result in the same value of Φ_Δ. It conveniently distills the information about the difference between the frames into a single value, but is also non-degenerate in the sense that $\Phi_\Delta = 0$ if and only if the frames are identical. It also reduces precisely to $\Phi_{\rm PN} - \Phi_{\rm NR}$ for non-precessing systems; for precessing systems it also incorporates contributions from the relative orientations of the orbital planes.[6]

Despite these useful features of Φ_Δ, it may sometimes be interesting to use different measures, to extract individual components of the binary evolution. For example, Eq. (1a) describes the precession of the orbital plane. When comparing this precession for two approaches, a more informative quantity than Φ_Δ is simply the angle between the $\hat{\ell}$ vectors in the two systems:

$$\angle L = \cos^{-1}\left(\hat{\ell}^{\rm PN}\cdot\hat{\ell}^{\rm NR}\right). \tag{12}$$

Similarly, we will be interested in understanding the evolution of the spin vectors, as given in Eqs. (2). For this purpose, we define the angles between the spin vectors:

$$\angle\chi_1 = \cos^{-1}\left(\hat{\chi}_1^{\rm PN}\cdot\hat{\chi}_1^{\rm NR}\right), \tag{13a}$$

[5] More explanation of these expressions, along with relevant formulas for calculating their values, can be found in Appendix B.

[6] It is interesting to note that any attempt to define the orbital phases of precessing systems separately, and then compare them as some $\Phi_B - \Phi_A$, is either ill defined or degenerate—as shown in Appendix B 4. This does not mean that it is impossible to define such phases, but at best they will be degenerate; multiple angles would be needed to represent the full dynamics.

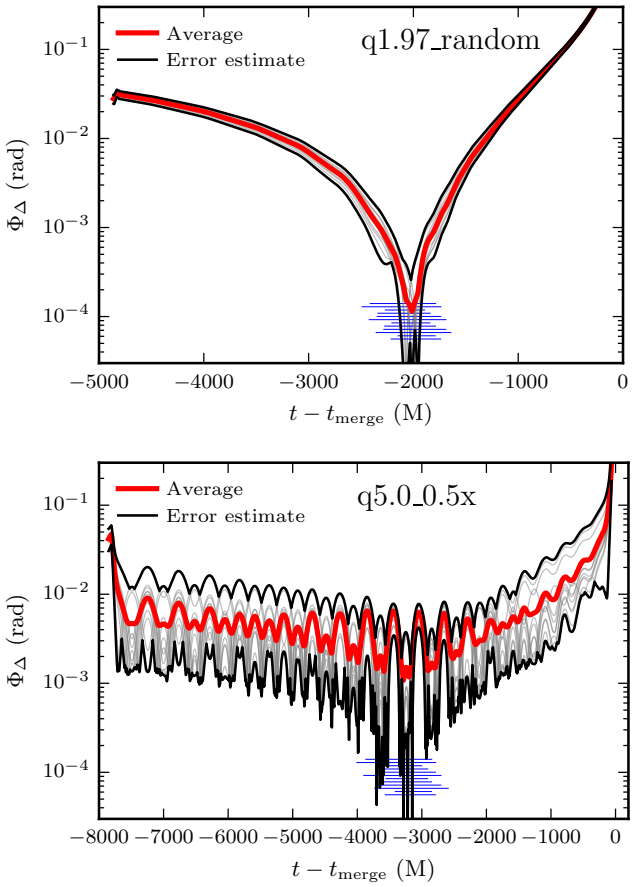

FIG. 3. Examples of the averaging procedure and error estimates employed for all comparisons. Shown here are q1.97_random and q5.0_0.5x. PN evolutions were performed with the Taylor T1 approximant. The thin blue lines show all the PN-NR matching intervals.

$$\angle\chi_2 = \cos^{-1}\left(\hat{\chi}_2^{\rm PN}\cdot\hat{\chi}_2^{\rm NR}\right). \tag{13b}$$

We will use all four of these angles below to compare the post-Newtonian and numerical orbital elements.

D. Matching Post-Newtonian to Numerical Relativity

When comparing PN theory to NR results, it is important to ensure that the initial conditions used in both cases represent the same physical situation. We choose a particular orbital frequency Ω_m and use the NR data to convert it to a time t_m. To initialize a PN evolution at t_m, we need to specify

$$q, \chi_1, \chi_2, \tag{14}$$
$$\hat{\ell}, \hat{n}, \hat{\chi}_1, \hat{\chi}_2, \tag{15}$$
$$\Omega. \tag{16}$$

The quantities (14) are conserved during the PN evolution. The quantities (15) determine the orientation of the the binary and its spins relative to the inertial triad $(\hat{x}, \hat{y}, \hat{z})$. The orbital frequency Ω in Eq. (16), finally, parametrizes the separation of the binary at t_m. The simplest approach is to initialize the PN evolution from the respective quantities in the initial data of the NR evolution. This would neglect initial transients in NR data as in, e.g., Fig. 1 of Ref. [40]. These transients affect the masses and spins of the black holes, so any further PN-NR comparisons would be comparing slightly different physical configurations. The NR transients decay away within the first orbit of the NR simulation, so one can consider initializing the PN evolution from NR at a time after the NR run has settled down. However, the generally non-zero (albeit very small) orbital eccentricity in the NR simulation can lead to systematic errors in the subsequent comparison as pointed out in Ref. [32].

Therefore, we use time-averaged quantities evaluated after the initial transients have vanished. In particular, given a numerical relativity simulation, we set the PN variables listed in Eq. (14) to their numerical relativity values after junk radiation has propagated away.

The remaining nine quantities Eqs. (15) and (16) must satisfy the constraint $\hat{\ell}\cdot\hat{n} \equiv 0$. We determine them with constrained minimization by first choosing an orbital frequency interval $[\Omega_m - \delta\Omega/2, \Omega_m + \delta\Omega/2]$ of width $\delta\Omega$. Computing the corresponding time interval $[t_i, t_f]$ in the NR simulation, we define the time average of any quantity Q by

$$\langle Q\rangle = \frac{1}{t_f - t_i}\int_{t_i}^{t_f} Q\, dt. \tag{17}$$

Using these averages, we construct the objective functional $\mathcal{S}$ as

$$\mathcal{S} = \langle(\angle L)^2\rangle + \langle(\angle\chi_1)^2\rangle + \langle(\angle\chi_2)^2\rangle + \langle(\Delta\Omega)^2\rangle \tag{18}$$

where $\Delta\Omega = (\Omega_{\rm PN} - \Omega_{\rm NR})/\Omega_{\rm NR}$. When a spin on the black holes is below 10^{-5} the corresponding term is dropped from Eq. (18). The objective functional is then minimized using the SLSQP algorithm [48, 49] to allow for constrained minimization. In Eq. (18) we use equal weights for each term; other choices of the weights do not change the qualitative picture that we present.

The frequency interval $[\Omega_m \pm \delta\Omega/2]$ is chosen based on several considerations. First it is selected after junk radiation has propagated away. Secondly, it is made wide enough so that any residual eccentricity effects average out. Finally, we would like to match PN and NR as early as possible. But since we want to compare various cases to each other, the lowest possible matching frequency will be limited by the shortest NR run (case q8_-0.5z). Within these constraints, we choose several matching intervals, in order to estimate the impact of the choice of matching interval on our eventual results. Specifically, we use three matching frequencies

$$m\Omega_m \in \{0.021067, 0.021264, 0.021461\}, \tag{19}$$

and employ four different matching windows for each, namely

$$\delta\Omega/\Omega_m \in \{0.06, 0.08, 0.1, 0.12\}. \quad (20)$$

These frequencies correspond approximately to the range between 10-27 orbits to merger depending on the parameters of the binary, with the lower limit for the case q1.0_-0.5x and the upper for q8.0_0.5x.

Matching at multiple frequencies and frequency windows allows an estimate on the error in the matching and also ensures that the results are not sensitive to the matching interval being used. In this article, we generally report results that are averaged over the 12 PN-NR comparisons performed with the different matching intervals. We report error bars ranging from the smallest to the largest result among the 12 matching intervals. As examples, Fig. 3 shows Φ_Δ as a function of time to merger $t_{\rm merge}$ for the cases q1.97_random and q5_0.5x for all the matching frequencies and intervals, as well as the average result and an estimate of the error. Here $t_{\rm merge}$ is the time in the NR simulation when the common horizon is detected.

III. RESULTS

A. Precession Comparisons

We apply the matching procedure of Sec. II D to the precessing NR simulations in Table I. PN–NR matching is always performed at the frequencies given by Eq. (19) which are the lowest feasible orbital frequencies across all cases in Table I. Figure 1 shows the precession cones for the normal to the orbital plane $\hat{\ell}$ and the spins $\hat{\chi}_{1,2}$. As time progresses, $\hat{\ell}$ and $\hat{\chi}_{1,2}$ undergo precession and nutation, and the precession cone widens due to the emission of gravitational radiation. Qualitatively, the PN results seem to follow the NR results well, until close to merger.

We now turn to a quantitative analysis of the precession dynamics, establishing first that the choice of Taylor approximant is of minor importance for the precession dynamics. We match PN dynamics to the NR simulations q5_0.5x and q1_0.5x for the Taylor approximants T1, T4 and T5. We then compute the angles $\angle L$ and $\angle\chi_1$. Figure 4 shows the resulting $\angle L$. During most of the inspiral, we find $\angle L$ of order a few 10^{-3} radians increasing to ~ 0.1 radians during the last $1000M$ before merger. Thus the direction of the normal to the orbital plane is reproduced well by PN theory. This result is virtually independent of the Taylor approximant suggesting that the choice of approximant only weakly influences how well PN precession equations track the motion of the orbital plane. In other words, precession dynamics does not depend on details of orbital phasing like the unmodeled higher-order terms in which the Taylor approximants differ from each other.

Turning to the spin direction $\hat{\chi}_1$ we compute the angle $\angle\chi_1$ between $\hat{\chi}_1^{\rm NR}(t)$ and $\hat{\chi}_1^{\rm PN}(t)$ and plot the result in Fig. 5. While Fig. 5 looks busy, the first conclusion is that $\angle\chi_1$ is quite small $\lesssim 0.01$ rad through most of the inspiral, and rises somewhat close to merger.

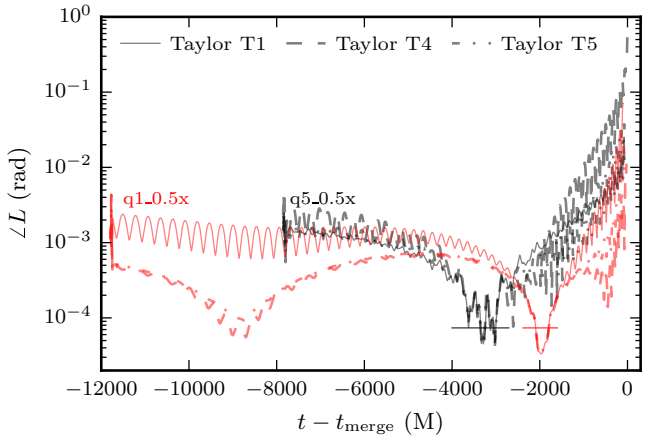

FIG. 4. Angle $\angle L$ by which $\hat{\ell}^{\rm PN}(t)$ differs from $\hat{\ell}^{\rm NR}(t)$ for the configuration q1_0.5x (red lines) and q5_0.5x (black lines). $\angle L \leq 0.2^\circ$ except very close to merger. In each case, the PN predictions based on different PN approximants are shown in different line styles. Shown is the point-wise average of 12 $\angle L(t)$ curves, i.e. the thick red line of Fig. 3. The thin horizontal lines show the widest edges of the PN matching intervals.

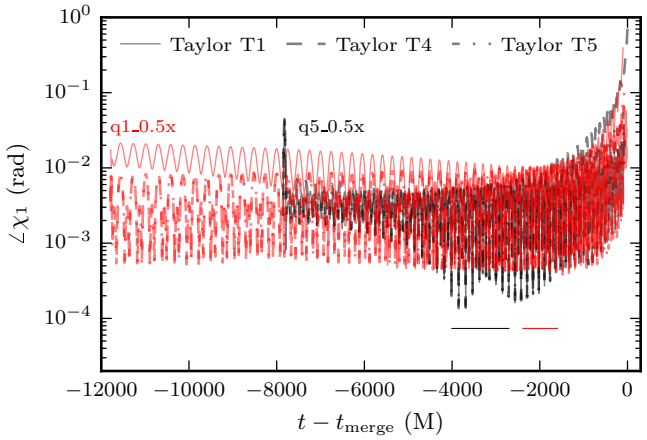

FIG. 5. Angle $\angle\chi_1$ by which $\vec{\chi}_1^{\rm PN}(t)$ differs from $\vec{\chi}_1^{\rm NR}(t)$ for the configuration q1_0.5x (red lines) and q5_0.5x (black lines). In each case, the PN predictions based on different PN approximants are shown in different line styles. The thin horizontal lines show the widest edges of the PN matching intervals.

The pronounced short-period oscillations of $\angle\chi_1$ in Fig. 5 are caused by differences between PN-nutation features and NR-nutation features. To better understand the nutation features and their impact on the angle $\angle\chi_1$, we remove nutation features by filtering out all frequencies comparable to the orbital frequency. This is possible because the precession frequency is much smaller than the nutation frequency. The filtering is performed with a 3rd order, bi-directional low pass Butterworth filter [50] with a fixed cutoff frequency chosen to be lower than the

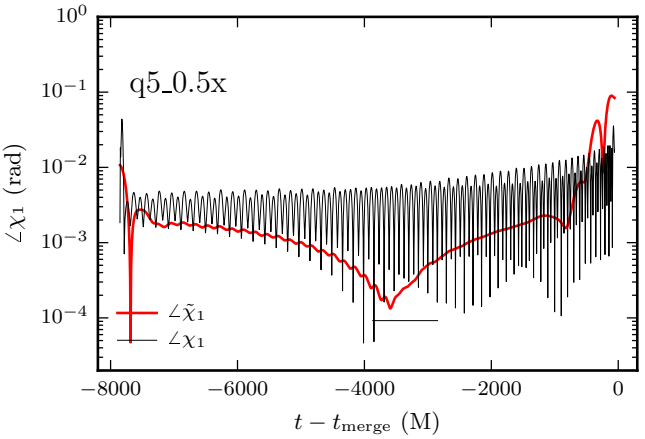

FIG. 6. Angle $\angle\tilde{\chi}_1$ between the "orbit-averaged" spins for the configuration q5_0.5x. The non orbit-averaged difference $\angle\chi_1$ (cf. Fig. 5) is shown for comparison. Shown is one matching interval as indicated by the thin horizontal line.

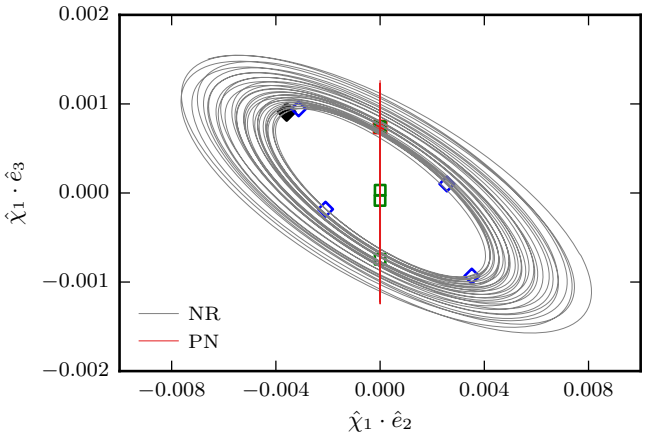

FIG. 7. The projection of $\hat{\chi}_1^{\rm NR}$ and $\hat{\chi}_1^{\rm PN}$ onto the $\hat{e}_2 - \hat{e}_3$ plane described in the text for case q5_0.5x. The system is shown in the interval $t - t_{\rm merge} \in [-6662, -1556]$. along the $\hat{e}_3$ axis. Meanwhile, the NR data show variations in $\hat{e}_2$ and $\hat{e}_3$ directions of comparable magnitude. The solid symbols (black diamond for NR, red square for PN) indicate the data at the start of the plotted interval, chosen such that $\hat{\chi}_1 \cdot \hat{n}$ is maximal—i.e., where the spin projection into the orbital plane is parallel to $\hat{n}$. The subsequent four open symbols (blue diamonds for NR, green squares for PN) indicating the position 1/8-th, 1/4-th, 3/8-th and 1/2 of an orbit later.

nutation frequency at the start of the inspiral. Due to the nature of the filtering, the resulting averaged spin will suffer from edge effects which affect approximately the first and last 1000 M of the inspiral. Furthermore, the precession frequency close to merger becomes comparable to the nutation frequency at the start of the simulation and thus filtering is no longer truthful in this region. Therefore, we only use the "averaged" spins where such features are absent.

Applying this smoothing procedure to both $\hat{\chi}_1^{\rm PN}$ and $\hat{\chi}_1^{\rm NR}$ for the run q5_0.5x, we compute the angle $\angle\tilde{\chi}_1$ between the averaged spin vectors, $\tilde{\chi}_1^{\rm PN}$ and $\tilde{\chi}_1^{\rm NR}$. This angle is plotted in Fig. 6[7], where results only for the Taylor T1 approximant are shown, and for only one matching interval specified by $m\Omega_m = 0.0210597$ and $\delta\Omega/\Omega_m = 0.1$. The orbit-averaged spin directions $\tilde{\chi}_1^{\rm NR/PN}$ agree significantly better with each other than the non-averaged ones (cf. the black line in Fig. 6, which is duplicated from Fig. 5). In fact, the orbit-averaged spin precessing between NR and PN agrees as well as the orbital angular momentum precession, cf. Fig. 4. Thus, the difference in the spin dynamics is dominated by the nutation features, with the orbit-averaged spin dynamics agreeing well between PN and NR.

To characterize the nutation features in the spin vectors, we introduce a coordinate system which is specially adapted to highlighting nutation effects. The idea is to visualize nutation with respect to the averaged spin vector $\tilde{\chi}$. We compute the time-derivative $\dot{\tilde{\chi}}$ numerically. Assuming that the "averaged" spin is undergoing pure precession, so that $\tilde{\chi} \cdot \dot{\tilde{\chi}} = 0$, we define a new coordinate system $(\hat{e}_1, \hat{e}_2, \hat{e}_3)$ by $\hat{e}_1 = \tilde{\chi}, \hat{e}_2 = \dot{\tilde{\chi}}/|\dot{\tilde{\chi}}|, \hat{e}_3 = \hat{e}_1 \times \hat{e}_2$. The spin is now projected onto the $\hat{e}_2 - \hat{e}_3$ plane, thus showing the motion of the spin in a frame "coprecessing" with the averaged spin. This allows us to approximately decouple precession and nutation and compare them separately between PN and NR.

Figure 7 plots the projection of the spins $\chi_1^{\rm NR}$ and $\chi_1^{\rm PN}$ onto their respective "orbit averaged" $\hat{e}_2 - \hat{e}_3$ planes. We see that the behavior of the NR spin and the PN spins are qualitatively different: For this single-spin system, the PN spin essentially changes only in the $\hat{e}_3$ direction (i.e., orthogonal to its average motion $\dot{\hat{\chi}}^{\rm PN}$). In contrast, the NR spin undergoes elliptical motion with the excursion along its $\hat{e}_2$ axis (i.e., along the direction of the average motion) about several times larger than the oscillations along $\hat{e}_3$. The symbols plotted in Fig. 7 reveal that each of the elliptic "orbits" corresponds approximately to half an orbit of the binary, consistent with the interpretation of this motion as nutation. The features exhibited in Fig. 8 are similar across all the single-spinning precessing cases considered in this work. The small variations in spin direction exhibited in Fig. 7 are orders of magnitude smaller than parameter estimation capabilities of LIGO, e.g. [51], and so we do not expect that these nutation features will have a negative impact on GW detectors.

Let us now apply our nutation analysis to the orbital angular momentum directions $\hat{\ell}$. Analogous to the spin, we compute averages $\tilde{\ell}^{\rm NR}$ and $\tilde{\ell}^{\rm PN}$, and compute the angle between the directions of the averages, $\angle\tilde{L} = \angle\left(\tilde{\ell}^{\rm PN}, \tilde{\ell}^{\rm NR}\right)$. This angle—plotted in the top panel of Fig. 8—agrees very well with the difference $\angle L$ that was computed without orbit-averaging. This indi-

[7] To illustrate edge effects of the Butterworth filter, Fig. 6 includes the early and late time periods where the filter affects $\angle\tilde{\chi}_1$.

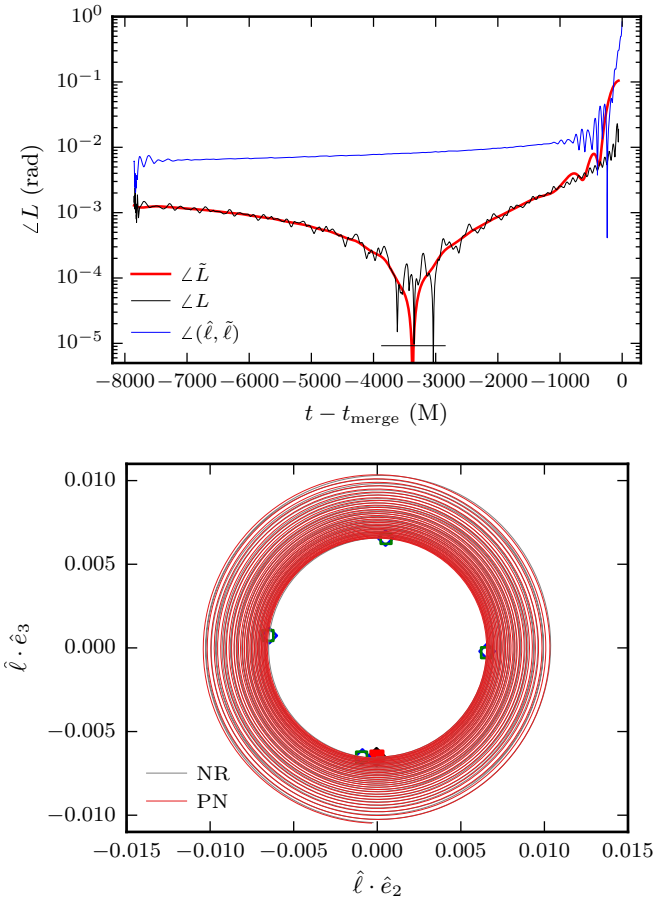

FIG. 8. Characterization of nutation effects of the orbital angular momentum. **Top**: angle $\angle\tilde{L}$ between the "averaged" $\hat{\ell}$ in PN and NR for the configuration q5_0.5x (thick red line). $\angle L$ is shown in thin black line for comparison (cf. Fig. 6). The thin blue line shows $\angle(\hat{\ell},\tilde{\ell})$ between the averaged and the filtered signal. Note that it is larger than both $\angle L$ and $\angle\tilde{L}$. **Bottom**: the projection of $\hat{\ell}^{\rm NR}$ (gray) and $\hat{\ell}^{\rm PN}$ (red) onto the $\hat{e}_2 - \hat{e}_3$ plane described in the text for case q5_0.5x (cf. Fig. 8). The system is shown in the interval $[-6662, -1556]$. Both PN and NR show the same behavior, in contrast to the behavior of the spin in Fig. 7. The PN-NR matching interval is indicated by the horizontal line in the top panel.

cates that the nutation features of $\hat{\ell}$ agree between NR and PN. The top panel of Fig. 9 also plots the angle between the raw $\hat{\ell}^{\rm NR}$ and the averaged $\tilde{\ell}^{\rm NR}$, i.e. the opening angle of the nutation oscillations. As is apparent in Fig. 8, the angle between $\hat{\ell}^{\rm NR}$ and $\tilde{\ell}^{\rm NR}$ is about 10 times larger than the difference between NR and PN ($\angle L$ or $\angle\tilde{L}$), confirming that nutation features are captured. The lower panel of Fig. 8 shows the projection of $\hat{\ell}$ orthogonal to the direction of the average $\tilde{\ell}$. In contrast to the spins shown in Fig. 7, the nutation behavior of $\hat{\ell}$ is in close agreement between NR and PN: For both, $\hat{\ell}$ precesses in a circle around $\tilde{\ell}$, with identical period, phasing, and with almost identical amplitude. We also point out that the shape of the nutation features differs between $\hat{\ell}$ and $\hat{\chi}_1$: $\hat{\ell}$ circles twice per orbit around its average $\tilde{\ell}$, on an almost perfect circle with equal amplitude in the $\hat{e}_2$ and $\hat{e}_3$ direction.

We now extend our precession dynamics analysis to the remaining five primary precessing NR simulations listed in Table I. The top left panel of Figure 9 shows $\angle L$. The difference in the direction of the normal to the orbital plane is small; generally $\angle L \lesssim 10^{-2}$ radians, except close to merger. Thus it is evident that the trends seen in Fig. 4 for $\angle L$ hold across all the precessing cases. To make this behavior clearer, we parameterize the inspiral using the orbital phase instead of time, by plotting the angles versus the orbital phase in the NR simulation, as shown in the top right panel of Fig. 9. Thus, until a few orbits to merger PN represents the precession and nutation of the orbital plane well.

The bottom left panel of Fig. 9 establishes qualitatively good agreement for $\angle\chi_1$, with slightly higher values than $\angle L$. As already illustrated in Fig. 6, nutation features dominate the difference. Averaging away the nutation features, we plot the angle $\angle\tilde{\chi}_1$ between the smoothed spins in the bottom left panel of Fig. 9, where the behavior of $\angle\chi_1$ is very similar to that of $\angle L$. This confirms that the main disagreement between PN and NR spin dynamics comes from nutation features, and suggests that the secular precession of the spins is well captured across all cases, whereas the nutation of the spins is not.

All configurations considered so far except q1.97_random have $\vec{S}\cdot\hat{\ell} = 0$ at the start of the simulations, where $\vec{S} = \vec{S}_1 + \vec{S}_2$ is the total spin angular momentum of the system. When $\vec{S}\cdot\hat{\ell} = 0$, several terms in PN equations vanish, in particular the spin orbit terms in the expansions of the binding energy, the flux and the orbital precession frequency, see Eqs. (A14), (A15), and (A31) in Appendix A.

To verify whether $\vec{S}\cdot\hat{\ell} = 0$ introduces a bias to our analysis, we perform our comparison on an additional set of 31 binaries with randomly oriented spins. These binaries have mass ratio $1 \le q \le 2$, spin magnitudes $0 \le \chi_{1,2} \le 0.5$, and correspond to cases SXS:BBH:0115 - SXS:BBH:0146 in the SXS catalog. Fig. 10 plots $\angle L$ for these additional 31 PN-NR comparisons in gray, with q1.97_random highlighted in orange. The disagreement between PN and NR is similarly small in all of these cases, leading us to conclude that our results are robust in this region of the parameter space.

B. Orbital Phase Comparisons

Along with the precession quantities described above, the orbital phase plays a key role in constructing PN waveforms. We use Φ_Δ, a geometrically invariant angle that reduces to the orbital phase difference for non-precessing binaries (cf. Sec. II C) to characterize phasing effects. We focus on single spin systems with mass-ratios from 1 to 8, where the more massive black hole carries a spin of $\chi_1 = 0.5$, and where the spin is aligned or anti-

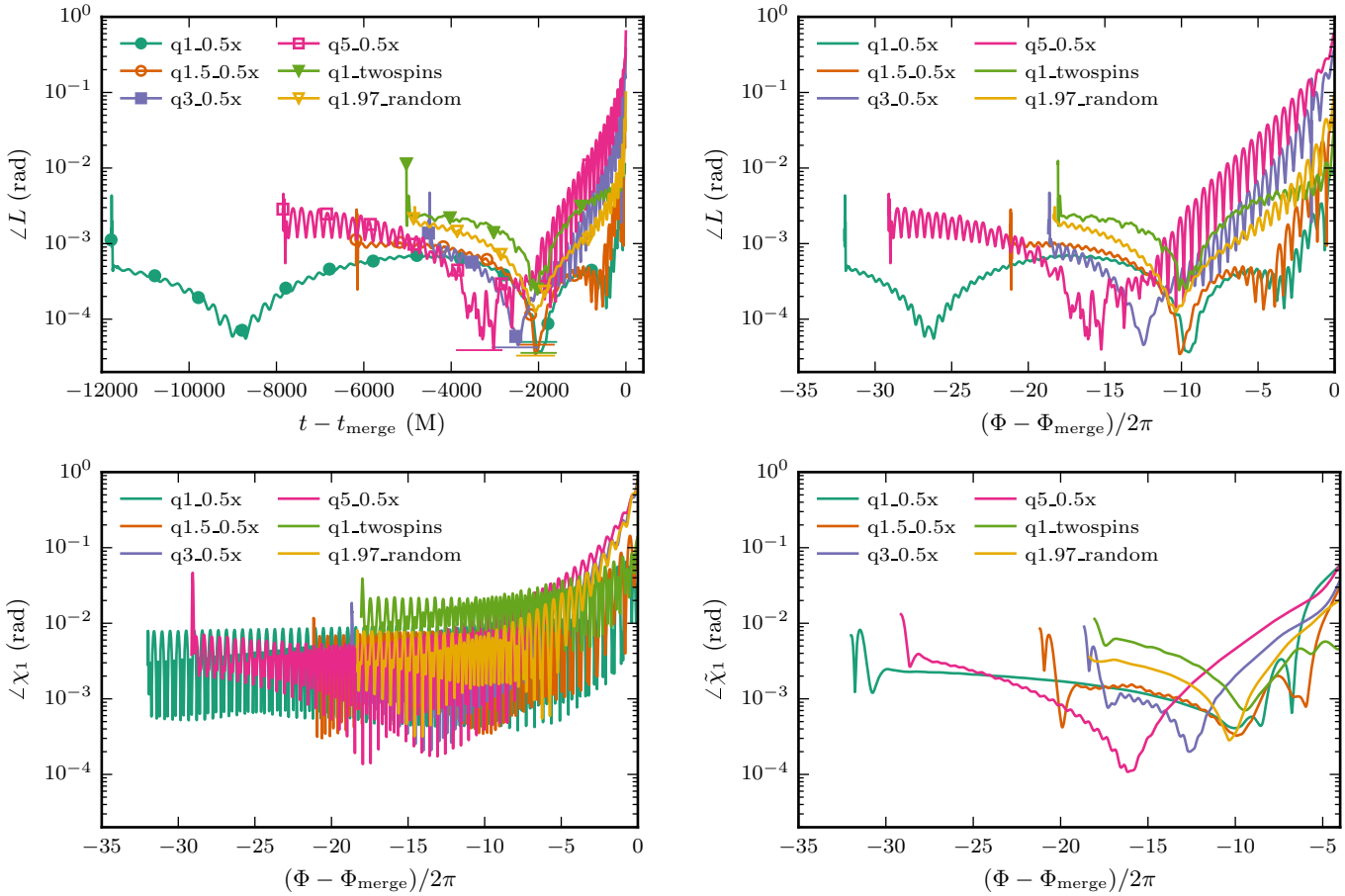

FIG. 9. Comparison of orbital plane and spin precession for the primary six precessing NR simulations. **Top Left**: $\angle L$ as a function of time to merger. **Top right**: $\angle L$ as a function of *orbital phase*. **Bottom left**: $\angle \chi_1$ as a function of orbital phase. **Bottom right**: $\angle \tilde{\chi}_1$ between the averaged spins. All data plotted are averages over 12 matching intervals, cf. Fig. 3, utilizing the Taylor T4 PN approximant. The thin horizontal lines in the top left panel show the widest edges of the PN matching intervals.

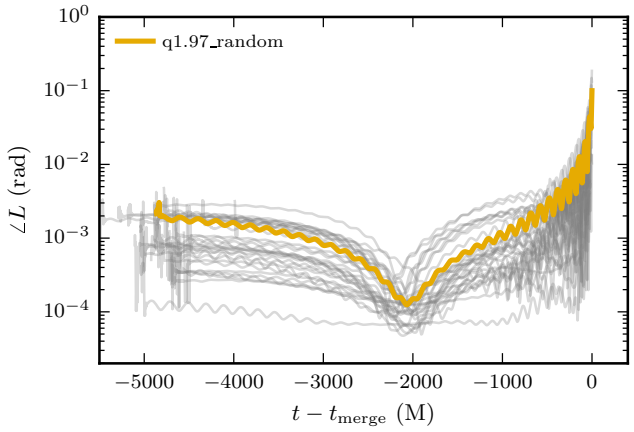

FIG. 10. $\angle L$ for additional 31 precessing configurations with arbitrary oriented spins as well as the case q1.97_random. Here $q \in (1, 2)$, $\chi_{1,2} \leq 0.5$. For all cases, $\angle L < 0.5^\circ$ throughout most of the inspiral. All data plotted are averages over 12 matching intervals, cf. Fig. 3.

aligned with the orbital angular momentum, or where the spin is initially tangent to the orbital plane. We match all NR simulations to post-Newtonian inspiral dynamics as described in Sec. II D, using the 12 matching intervals specified in Eqs. (19) and (20). We then compute the phase difference Φ_Δ at the time at which the NR simulation reaches orbital frequency $m\Omega = 0.3$.

The results are presented in Fig. 11, grouped based on the initial orientation of the spins: aligned, anti-aligned, and in the initial orbital plane. For aligned runs, there are clear trends for Taylor T1 and T5 approximants: for T1, differences decrease with increasing mass ratio (at least up to $q = 8$); for T5, differences increase. For Taylor T4, the phase difference Φ_Δ has a minimum and there is an overall increase for higher mass ratios. For anti-aligned runs, Taylor T5 shows the same trends as for the aligned spins. Taylor T4 and T1 behaviors, however, have reversed: T4 demonstrates a clear increasing trend with mass ratio, whereas T1 passes through a minimum with overall increases for higher mass ratios. Our results are also qualitatively consistent with the results described

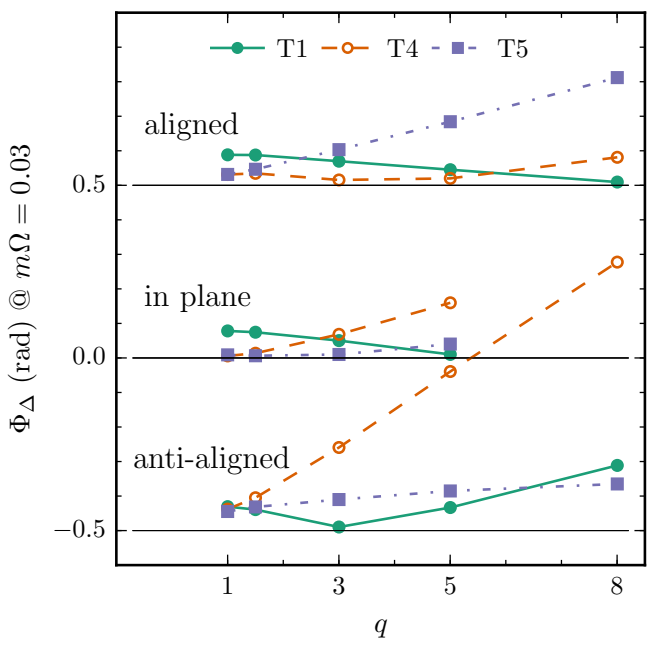

FIG. 11. Φ_Δ as a function of mass ratio for BBH systems with $\chi_1 = 0.5$, and spin direction aligned (top), orthogonal (middle), and anti-aligned (bottom) with the orbital angular momentum. For clarity, the aligned/anti-aligned data are offset by $+0.5$ and -0.5, respectively, with the thin horizontal black lines indicating zero for each set of curves. Plotted is Φ_Δ averaged over the 12 matching intervals, cf. Fig. 3, and for three different Taylor approximants.

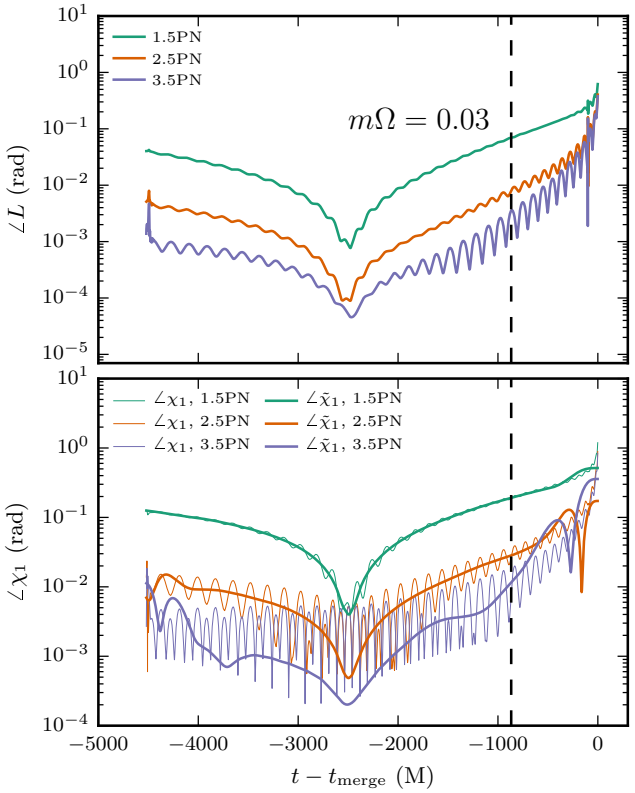

FIG. 12. Comparison of PN-NR precession dynamics when the expansion order of the PN precession equations is varied. Shown is the case q3_0.5x. The top panel shows the precession of the orbital plane, and the bottom panel of the spin $\hat{\chi}_1$ (without and with averaging). All data shown are averages over 12 matching intervals, cf. Fig. 3.

in [52] as we find that for equal mass binaries, the Taylor T4 approximant performs better than the Taylor T1 approximant (both for aligned and anti-aligned spins).

For the in-plane precessing runs, we see clear trends for all 3 approximants: Taylor T4 and T5 both show increasing differences with increasing mass ratio, and T1 shows decreasing differences. These trends for precessing binaries are consistent with previous work on non-spinning binaries [13], which is expected since for $\vec{S}\cdot\hat{\ell}$ many of the same terms in the binding energy and flux vanish as for non-spinning binaries. Overall, we find that for different orientations and mass ratios, no one Taylor approximant performs better than the rest, as expected if the differences between the approximants arise from different treatment of higher-order terms.

C. Convergence with PN order

So far all comparisons were performed using all available post-Newtonian information. It is also instructive to consider behavior at different PN order, as this reveals the convergence properties of the PN series, and allows estimates of how accurate higher order PN expressions might be.

The precession frequency ϖ, given in Eq. (A31), is a product of series in the frequency parameter x. We multiply out this product, and truncate it at various PN orders from leading order (corresponding to 1.5PN) through next-to-next-to-leading order (corresponding to 3.5PN). Similarly, the spin precession frequencies $\vec{\Omega}_{1,2}$ in Eqs. (2) and (A32) are power series in x. We truncate the power series for $\vec{\Omega}_{1,2}$ in the same fashion as the power series for ϖ, but keep the orbital phase evolution at 3.5PN order, where we use the TaylorT4 prescription to implement the energy flux balance. For different precession-truncation orders, we match the PN dynamics to the NR simulations with the same techniques and at the same matching frequencies as in the preceding sections.

When applied to the NR simulation q3_0.5x, we obtain the results shown in Fig. 12. This figure shows clearly that with increasing PN order in the precession equations, PN precession dynamics tracks the NR simulation more and more accurately. When only the leading order terms of the precession equations are included (1.5PN order), $\angle L$ and $\angle\chi_1$ are ≈ 0.1rad; at 3.5PN order this difference drops by nearly two orders of magnitude.

We repeat this comparison for our six main precessing cases from Table I. The results are shown in Fig. 13. It is evident that for *all cases* $\angle L$ decreases with increasing order in the precession equations with almost 2 orders of

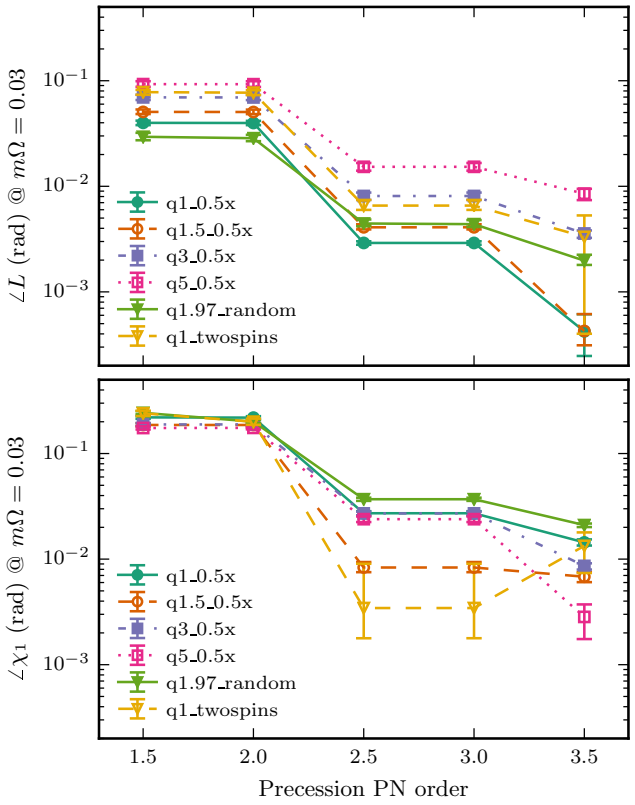

FIG. 13. Convergence of the PN precession equations for all cases in Table I. The evolution was done with the Taylor T4 approximant at 3.5 PN order. The leading order spin-orbit correction is at 1.5 PN order and the spin-squared corrections appear at 2 PN order. Each data point is the average $\angle L$ over PN-NR comparisons performed using 12 matching intervals, cf. Fig. 3, with error bars showing the maximal and minimal $\angle L$ and $\angle\chi_1$ of the 12 fits.

magnitude improvement between leading order and next-to-next leading order truncations. A similar trend is seen in the convergence of the spin angle $\angle\chi_1$ shown in bottom panel of Fig. 13. The angle decreases with PN order almost monotonically for all cases except q1.0_twospins. However, this is an artificial consequence of picking a particular matching point at $m\Omega = 0.03$: as can be seen from the bottom panel of Fig. 12 $\angle\chi_1$ shows large oscillations and it is a coincidence that the matching point happens to be in a "trough" of χ_1.

So far we have varied the PN order of the precession equations, while keeping the orbital frequency evolution at 3.5PN order. Let us now investigate the opposite case: varying the PN order of the orbital frequency and monitoring its impact on the orbital phase evolution. We keep the PN order of the precession equations at 3.5PN, and match PN with different orders of the orbital frequency evolution (and TaylorT4 energy-balance prescription) to the NR simulations. We then evaluate Φ_Δ (a quantity that reduces to the orbital phase difference in cases where the latter is unambiguously defined) at the time at which the NR simulation reaches the frequency $m\Omega = 0.03$. We examine our six primary precessing runs, and also the aligned-spin and anti-aligned spin binaries listed in Table I.

When the spin is initially in the orbital plane, as seen in the top panel of Fig. 14, the overall trend is a non-monotonic error decrease with PN order, with spikes at 1 and 2.5 PN orders as has been seen previously with non-spinning binaries [32]. All of the aligned cases show a large improvement at 1.5 PN order, associated with the leading order spin-orbit contribution. The phase differences then spike at 2 and 2.5 PN orders and then decrease at 3 PN order. Finally, different cases show different results at 3.5 PN with some showing decreases differences while for others the differences increase.

For the anti-aligned cases the picture is similar to precessing cases with a spike at 1 and 2.5 PN orders and monotonic improvement thereafter. The main difference from precessing cases is the magnitude of the phase differences, which is larger by a factor of ~ 5 at 3.5 PN order for the anti-aligned cases (see for example q1.5_s0.5x_0).

These results suggest that convergence of the orbital phase evolution depends sensitively on the exact parameters of the system under study. Further investigation of the parameter space is warranted.

D. Impact of PN spin truncation

As mentioned in Sec. II A 2, post-Newtonian expansions are not fully known to the same orders for spin and non-spin terms. Thus, for example, the expression for flux $\mathcal{F}$ is complete to 3.5 PN order for non-spinning systems, but spinning systems may involve unknown terms at 2.5 PN order; a similar statement holds for dE/dx. This means that when the ratio in Eq. (4), $\mathcal{F}/(dE/dx)$, is re-expanded as in the T4 approximant, known terms will mix with unknown terms. It is not clear, *a priori*, how such terms should be handled when truncating that re-expanded series.

Here we examine the effects of different truncation strategies. We focus on the Taylor T4 approximant while considering various possible truncations of the re-expanded form of $\mathcal{F}/(dE/dx)$. We denote these possibilities by the orders of (1) the truncation of non-spin terms, (2) the truncation of spin-linear terms, and (3) the truncation of spin-quadratic terms. Thus, for example, in the case where we keep non-spin terms to 3.5 PN order, keep spin-linear terms to 2.5 PN order, and keep spin-quadratic terms only to 2.0 PN order, we write (3.5, 2.5, 2.0). We consider the following five possibilities:

(i) (3.5, 3.5, 3.5)
(ii) (3.5, 4.0, 4.0)
(iii) (3.5, 2.5, 2.0)
(iv) (3.5, 3.5, 2.0)
(v) (3.5, 4.0, 2.0).

To increase the impact of the spin-orbit terms, we examine aligned and anti-aligned cases from Table I, with results presented in Fig. 15. For aligned cases, no

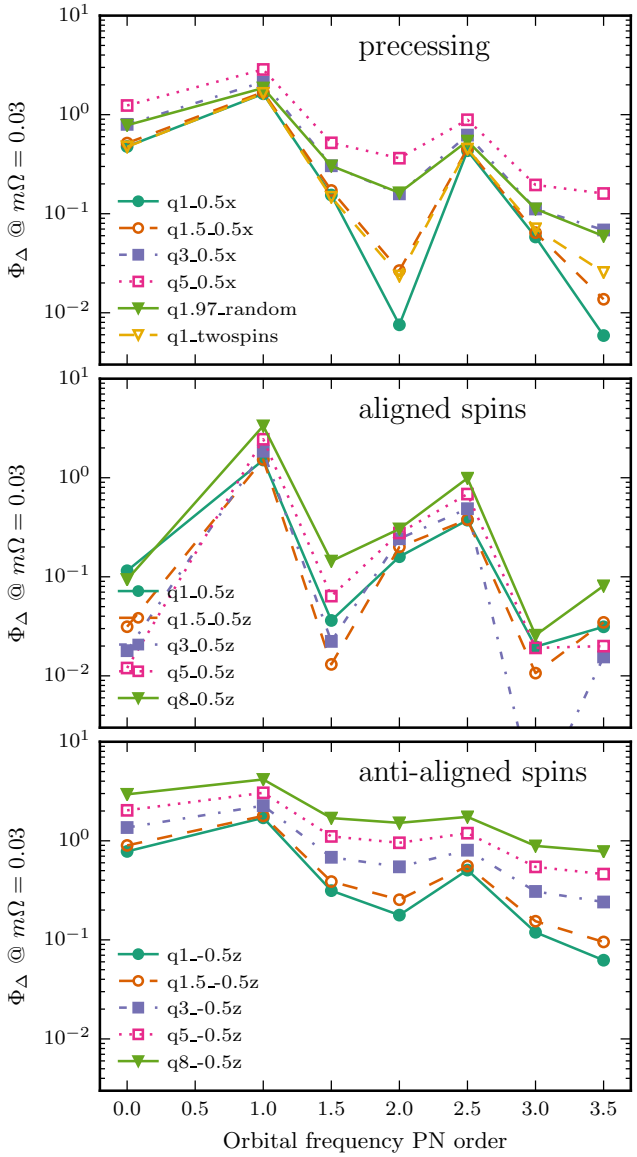

FIG. 14. Convergence of the Taylor T4 approximant with PN order. Shown are all cases from Table I. **Top**: all precessing cases. **Middle**: aligned spin cases. **Bottom**: anti-aligned spin cases. Each data point shown is averaged over PN-NR comparison with 12 matching intervals, cf. Fig. 3. Error bars are omitted for clarity, but would be of similar size to those in Fig. 15.

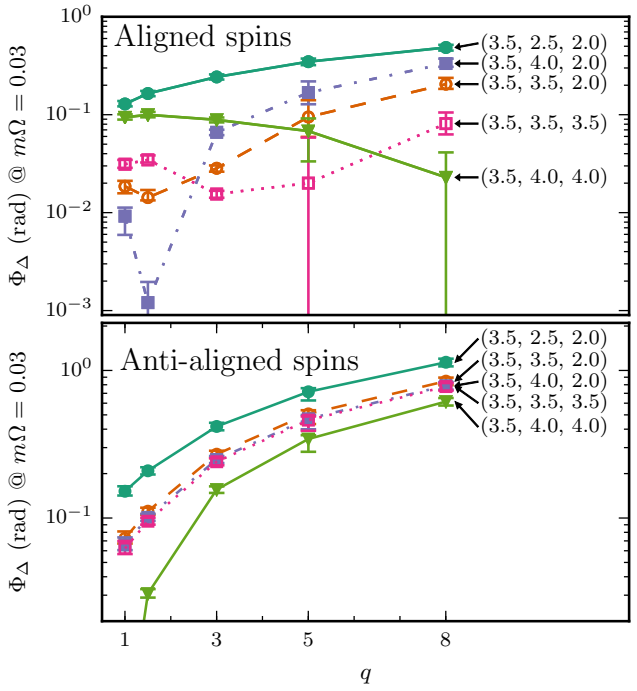

FIG. 15. Impact of different choices for spin truncation on orbital phase difference Φ_Δ, as a function of mass ratio. The lines are labeled by the truncation types, as explained in the text. The upper panel shows all cases for which the spins are aligned with the orbital angular momentum; the lower panel shows the anti-aligned cases.

one choice of spin truncation results in small differences across all mass ratios. All choices of spin truncation excepting (3.5, 4.0, 4.0) have increasing errors with increasing mass ratio. Truncating spin corrections at 2.5 PN order (3.5, 2.5, 2) consistently results in the worst matches. On the other hand, we find that, for anti-aligned runs, adding higher order terms always improves the match, keeping all terms yields the best result, and all choices of truncation give errors which are monotonically increasing with mass ratio. Overall, anti-aligned cases have larger values of Φ_Δ when compared to cases with same mass ratios. This result is consistent with findings by Nitz et al. [14] for comparisons between TaylorT4 and EOB-NRv1 approximants.

E. Further numerical considerations

1. *Numerical truncation error*

Still to be addressed is the effect of the resolution of NR simulations in the present work. The simulation q1_twospins is available at four different resolutions labeled N1, N2, N3 and N4. We match each of these four numerical resolutions with the Taylor T4 approximant, and plot the resulting phase differences Φ_Δ in Fig. 16 as the data with symbols and error bars (recall that the error bars are obtained from the 12 different matching regions we use, cf. Fig. 3). All four numerical resolutions yield essentially the same Φ_Δ. We furthermore match the three lowest numerical resolutions against the highest numerical resolution N4 and compute the phase difference Φ_Δ. The top panel of Figure 16 shows Φ_Δ computed with these 4 different numerical resolutions. All the curves lie on top of each other and the differences between them are well within the uncertainties due to the matching procedure. The bottom panel shows the differences in Φ_Δ between the highest resolution and all

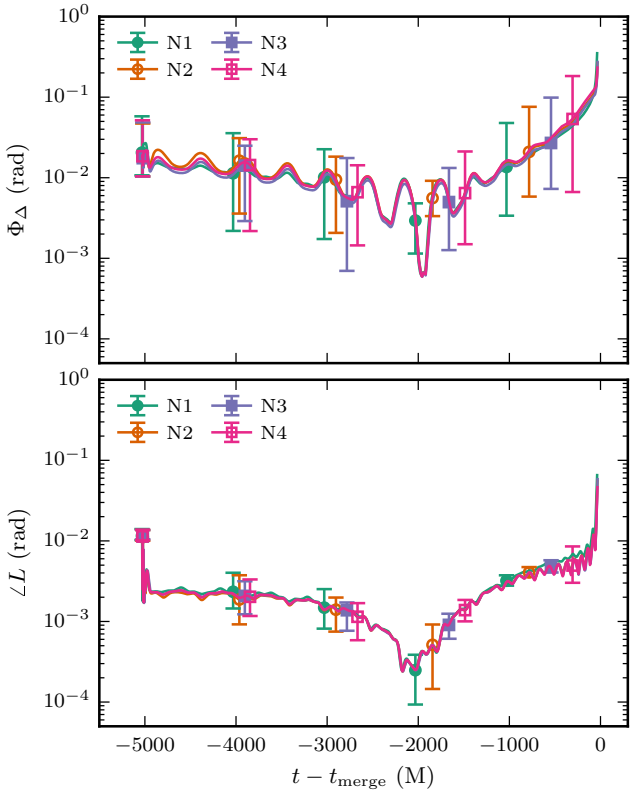

FIG. 16. Convergence test with the numerical resolution of the NR simulation q1_twospins. **Top panel**: Φ_Δ with comparisons done at different resolutions. All the curves lie within uncertainties due to the matching procedure, indicating that numerical truncation error does is not important in this comparison. The difference between each curve and the highest resolution are of order 15% and are within the matching uncertainties. **Bottom panel**: $\angle L$ with comparisons done at all the resolutions. The curves lie within the matching uncertainties.

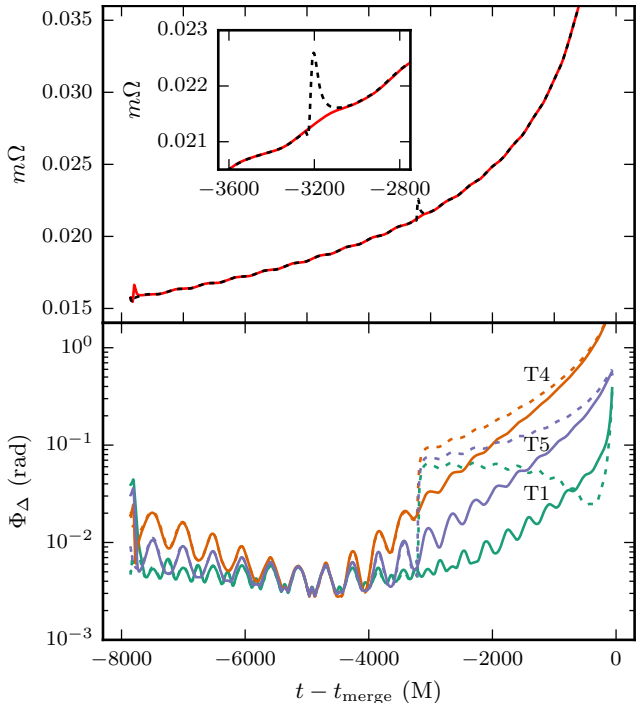

FIG. 17. Gauge change during numerical simulation q5_s0.5x. The solid curves represent the recent re-run of q5_0.5x that is analyzed in the rest of this paper. The dashed curves represent an earlier run SXS:BBH:0058 which changes the gauge at $t - t_{\rm merge} \approx -3200M$. **Top**: behavior of the orbital frequency $m\Omega$ in evolution with (dashed curve) and without gauge change (solid curve). **Bottom:** Φ_Δ for all Taylor approximants. To avoid matching during the gauge change, the matching was done with $m\Omega_c = 0.017$.

others. Throughout most of the inspiral, the difference is $\sim 10\%$. Similar behavior is observed in other cases where multiple resolutions of NR simulations are available. We therefore conclude that the effects of varying numerical resolution do not impact our analysis.

2. *Numerical gauge change*

The simulation SXS:BBH:0058 in the SXS catalog uses identical BBH parameters than q5_0.5x, but suffers from two deficiencies, exploration of which will provide some additional insights. First, the switch from generalized harmonic gauge with *fixed* gauge-source functions [32] to *dynamical* gauge-source functions [41, 42] happens near the middle of the inspiral, rather than close to merger as for the other simulations considered. This will give us an opportunity to investigate the impact of such a gauge change, the topic of this subsection. Second, this simulation also used too low resolution in the computation of the black hole spin during the inspiral, which we will discuss in the next subsection. We emphasize that the comparisons presented above did not utilize SXS:BBH:0058, but rather a re-run with improved technology. We use SXS:BBH:0058 in this section to explore the effects of its deficiencies.

While the difference between PN and NR gauges does not strongly impact the nature of the matching results, a gauge change performed during some of the runs *does* result in unphysical behavior of physical quantities such as the orbital frequency. Figure 17 demonstrates this for case q5_s0.5x. The old run SXS:BBH:0058 with the gauge change exhibits a bump in the orbital frequency (top panel), which is not present in the re-run (solid curve). When matching both the old and the new run to PN, and computing the phase difference Φ_Δ, the old run exhibits a nearly discontinuous change in Φ_Δ (bottom panel, dashed curves) while no such discontinuity is apparent in the re-run.

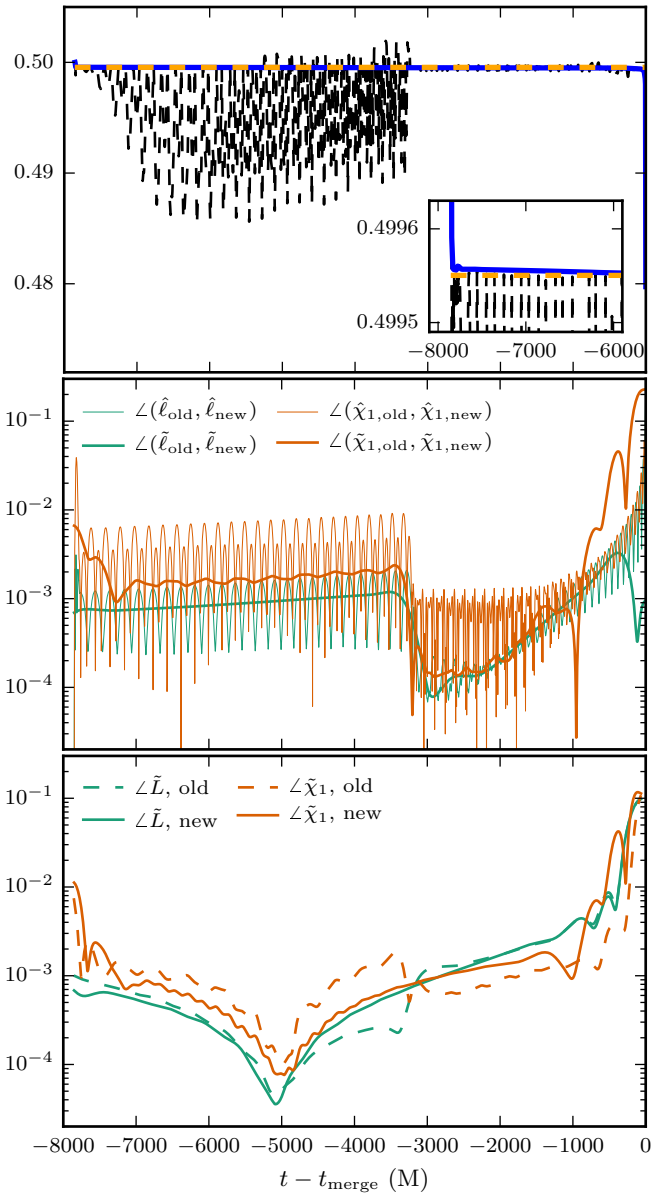

FIG. 18. **Top**: The magnitude of the spin as a function of time in the original run (black) and the new run (blue) as well as the value computed with the procedure described in the text (orange). **Middle panel**: angles between the spins and normals to the orbital plane (thin curves) and their averaged values (bold curves) for the original run and the re-run. **Lower panel**: $\angle\tilde{\chi}_1$ and $\angle\tilde{\ell}$ for both the old run and the re-run (the data of this panel are averaged over 12 matching intervals, cf. Fig. 3). To avoid matching during the gauge change, the matching was done with $m\Omega_c = 0.017$.

3. *Problems in quasi-local quantities*

Computation of the quasi-local spin involves the solution of an eigenvalue problem on the apparent horizon followed by an integration over the apparent horizon, cf. [53–55]. In the simulations q1.0_0.5x, q1.5_0.5x and q3.0_0.5x and in SXS:BBH:0058 (corresponding to q5_0.5x), too low numerical resolution was used for these two steps. While the evolution itself is acceptable, the extracted spin shows unphysical features. Most importantly, the reported spin magnitude is not constant, but varies by several per cent. Figure 18 shows as example χ_1 from SXS:BBH:0058. For $t - t_{\rm merge} \leq 3200M$ oscillations are clearly visible. These oscillations vanish at $t - t_{\rm merge} \approx 3200M$, coincident with a switch to damped harmonic gauge (cf. Sec. III E 2). Similar oscillations in q3_0.5 disappear when the resolution of the spin computation is manually increased about 1/3 through the inspiral, without changing the evolution gauge. Our new rerun q5_0.5x (using damped harmonic gauge throughout), also reports a clean χ_1, cf. Fig. 18. Thus, we conclude that the unphysical variations in the spin magnitude are only present if *both* the resolution of the spin computation is low, and the old gauge conditions of constant H_a are employed.

The NR spin magnitude is used to initialize the PN spin magnitude, cf. Eq. (14). Therefore, an error in the calculation of the NR spin would compromise our comparison with PN. For the affected runs, we correct the spin reported by the quasi-local spin computation by first finding all maxima of the spin-magnitude χ between $500M$ and $2000M$ after the start of the numerical simulation. We then take the average value of χ at those maxima as the corrected spin-magnitude of the NR simulation. Figure 18 shows the case q5_0.5x as well as the rerun described in Sec. III E 2. It is evident that this procedure produces a spin value which is very close to the spin in the rerun where the problematic behavior is no longer present. Thus, we adopt it for the three cases where an oscillation in the spin magnitude is present.

The nutation features shown in Fig. 7 are qualitatively similar for all our simulations, independent of resolution of the spin computation and evolution gauge. When the spin is inaccurately measured, the nutation trajectory picks up extra modulations, which are small on the scale of Fig. 7 and do not alter the qualitative behavior.

The lower two panels of Fig. 18 quantify the impact of inaccurate spin measurement on the precession-dynamics comparisons performed in this paper: The middle panel shows the differences between the spin directions in the original 0058 run and our re-run q5_0.5x. The spin directions differ by as much as 0.01 radians. However, as the lower panel shows, this difference can mostly be absorbed by the PN matching, so that $\angle\chi_1$ and $\angle L$ are of similar magnitude of about 10^{-3} radians.

IV. DISCUSSION

We have presented an algorithm for matching PN precession dynamics to NR simulations which uses constrained minimization. Using this algorithm, we perform a systematic comparison between PN and NR for precessing binary black hole systems. The focus of the comparison is black hole dynamics only, and we defer discussion

of waveforms to future work. By employing our matching procedure, we find excellent agreement between PN and NR for the precession and nutation of the orbital plane. The normals to the orbital plane generally lie within 10^{-2} radians, cf. Fig. 9. Moreover, nutation features on the orbital time-scale also agree well between NR and PN, cf. Fig. 8.

For the black hole spin direction, the results are less uniform. The NR spin direction $\hat{\chi}_1^{\rm NR}$ shows nutation features that are qualitatively different than the PN nutation features, cf. Fig. 7. The disagreement in nutation dominates the agreement of $\hat{\chi}_1^{\rm NR}$ with $\hat{\chi}_1^{\rm PN}$; averaging away the nutation features substantially improves agreement, cf. Fig. 6. The orbit-averaged spin directions agree with PN to the same extent that the $\hat{\ell}$ direction does (with and without orbit averaging), cf. Fig. 9.

Turning to the convergence properties of PN, we have performed PN-NR comparisons at different PN order of the precession equations. For both orbital angular momentum $\hat{\ell}$ and the spin direction $\hat{\chi}_1$, we observe that the convergence of the PN results toward NR is fast and nearly universally monotonic, cf. Fig. 13. At the highest PN orders, the spin results might be dominated by the difference in nutation features between PN and NR.

The good agreement between PN and NR precession dynamics are promising news for gravitational wave modeling. Precessing waveform models often rely on the post-Newtonian precession equations, e.g. [15, 56]. Our results indicate that the PN precession equations are well suited to model the precessing frame, thus reducing the problem of modeling precessing waveforms to the modeling of orbital phasing only.

The accuracy of the PN orbital phase evolution, unfortunately, does not improve for precessing systems. Rather, orbital phasing errors are comparable between non-precessing and precessing configurations, cf. Fig. 14. Moreover, depending on mass-ratio and spins, some Taylor approximants match the NR data particularly well, whereas others give substantially larger phase differences, cf. Fig. 11. This confirms previous work [9, 12, 13, 33, 57] that the PN truncation error of the phase evolution is important for waveform modeling.

We have also examined the effects of including partially known spin contributions to the evolution of the orbital frequency for the Taylor T4 approximant. For aligned runs, including such incomplete information usually improves the match, but the results are still sensitive to the mass ratio of the binary (top panel of Fig 15). For anti-aligned runs, it appears that incomplete information always improves the agreement of the phasing between PN and NR (bottom panel of Fig 15).

In this work we compare gauge-dependent quantities, and thus must examine the impact of gauge choices on the conclusions listed above. We consider it likely that the different nutation features of $\hat{\chi}_1$ are determined by different gauge choices. We have also seen that different NR gauges lead to measurably different evolutions of $\hat{\chi}$, $\hat{\ell}$, and the phasing, cf. Fig. 17 and 18. We expect, however, that our conclusions are fairly robust to the gauge ambiguities for two reasons. First, in the matched PN-NR comparison, the impact of gauge differences is quite small, cf. lowest panel of Fig. 18. Second, the near universal, monotonic, and quick convergence of the precession dynamics with precession PN order visible in Fig. 13 would not be realized if the comparison were dominated by gauge effects. Instead, we would expect PN to converge to a solution *different* from the NR data.

ACKNOWLEDGMENTS

We thank Kipp Cannon, Francois Foucart, Prayush Kumar, Abdul Mroué and Aaron Zimmerman for useful discussions. Calculations were performed with the SpEC-code [58]. We gratefully acknowledge support from NSERC of Canada, from the Canada Research Chairs Program, and from the Canadian Institute for Advanced Research. We further gratefully acknowledge support from the Sherman Fairchild Foundation; from NSF Grants PHY-1306125 and AST-1333129 at Cornell; and from NSF Grants No. PHY-1440083 and AST-1333520 at Caltech. Calculations were performed at the GPC supercomputer at the SciNet HPC Consortium [59]; SciNet is funded by: the Canada Foundation for Innovation (CFI) under the auspices of Compute Canada; the Government of Ontario; Ontario Research Fund (ORF) – Research Excellence; and the University of Toronto. Further computations were performed on the Zwicky cluster at Caltech, which is supported by the Sherman Fairchild Foundation and by NSF award PHY-0960291; and on the NSF XSEDE network under grant TG-PHY990007N.

Appendix A: Post-Newtonian dynamics

We consider compact object binary with masses $m_{1,2}$ and carrying angular momentum $\vec{S}_{1,2}$. The post-Newtonian expressions are most conveniently written using the following symbols:

$$m = m_1 + m_2, \tag{A1}$$
$$\nu = \frac{m_1 m_2}{m^2}, \tag{A2}$$
$$\delta = \frac{m_1 - m_2}{m}, \tag{A3}$$
$$\vec{S} = \vec{S}_1 + \vec{S}_2, \tag{A4}$$
$$s_l = \frac{\vec{S}\cdot\hat{\ell}}{m^2}, \tag{A5}$$
$$s_n = \frac{\vec{S}\cdot\hat{n}}{m^2}, \tag{A6}$$
$$\vec{\Sigma} = \frac{m}{m_2}\vec{S}_2 - \frac{m}{m_1}\vec{S}_1, \tag{A7}$$
$$\sigma_l = \frac{\vec{\Sigma}\cdot\hat{\ell}}{m^2}, \tag{A8}$$

$$\sigma_n = \frac{\vec{\Sigma}\cdot\hat{n}}{m^2}, \tag{A9}$$

$$\vec{\chi}_s = \frac{1}{2}\left(\vec{\chi}_1 + \vec{\chi}_2\right), \tag{A10}$$

$$\vec{\chi}_a = \frac{1}{2}\left(\vec{\chi}_1 - \vec{\chi}_2\right), \tag{A11}$$

$$\vec{S}_0 = \frac{m}{m_1}\vec{S}_1 + \frac{m}{m_2}\vec{S}_2, \tag{A12}$$

$$\vec{s}_0 = \frac{\vec{S}_0}{m^2}. \tag{A13}$$

1. Energy and Flux

The energy and flux are written as power series in the expansion parameter $x \equiv (m\Omega)^{2/3}$:

$$E(x) = -\tfrac{1}{2}\, m\nu x \left(1 + \textstyle\sum_{k=2} a_k x^{k/2}\right), \tag{A14}$$

$$\mathcal{F}(x) \;= \tfrac{32}{5}\nu^2 x^5 \left(1 + \textstyle\sum_{k=2} b_k x^{k/2}\right). \tag{A15}$$

For the energy, coefficients are given explicitly by:

$$a_2 = -\frac{3}{4} - \frac{\nu}{12}, \tag{A16}$$

$$a_3 = 2\delta\sigma_l + \frac{14}{3}s_l, \tag{A17}$$

$$a_4 = -\frac{27}{8} + \frac{19}{8}\nu - \frac{1}{24}\nu^2 + \nu(\vec{\chi}_s^2 - \vec{\chi}_a^2 - 3[(\vec{\chi}_s\cdot\hat{\ell})^2 - (\vec{\chi}_a\cdot\hat{\ell})^2] + (\frac{1}{2} - \nu)\{\vec{\chi}_s^2 + \vec{\chi}_a^2 - 3[(\vec{\chi}_s\cdot\hat{\ell})^2 + (\vec{\chi}_a\cdot\hat{\ell})^2]\} + \delta\{\vec{\chi}_s\cdot\vec{\chi}_a - 3[(\vec{\chi}_s\cdot\hat{\ell})(\vec{\chi}_a\cdot\hat{\ell})]\}, \tag{A18}$$

$$a_5 = 11 s_l + 3\delta\sigma_l + \nu\left[-\frac{61}{9}s_l - \frac{10}{3}\delta\sigma_l\right], \tag{A19}$$

$$a_6 = -\frac{675}{64} + \left[\frac{34445}{576} - \frac{205}{96}\pi^2\right]\nu - \frac{155}{96}\nu^2 - \frac{35}{5184}\nu^3, \tag{A20}$$

$$a_7 = \left(\frac{135}{4} - \frac{367}{4}\nu + \frac{29}{12}\nu^2\right)s_l + \delta\left(\frac{27}{4} - 39\nu + \frac{5}{4}\nu^2\right)\sigma_l. \tag{A21}$$

Meanwhile for the flux $\mathcal{F}$:

$$b_2 = -\frac{1247}{336} - \frac{35}{12}\nu, \tag{A22}$$

$$b_3 = 4\pi - 4 s_l - \frac{5}{4}\delta\sigma_l, \tag{A23}$$

$$b_4 = -\frac{44711}{9072} + \frac{9271}{504}\nu + \frac{65}{18}\nu^2 + \left(\frac{287}{96} + \frac{\nu}{24}\right)(\vec{\chi}_s\cdot\hat{\ell})^2 - \left(\frac{89}{96} + \frac{7\nu}{24}\right)\vec{\chi}_s^2 + \left(\frac{287}{96} - 12\nu\right)(\vec{\chi}_a\cdot\hat{\ell})^2 + \left(-\frac{89}{96} + 4\nu\right)\vec{\chi}_a^2 + \frac{287}{48}\delta(\vec{\chi}_s\cdot\hat{\ell})(\vec{\chi}_a\cdot\hat{\ell}) - \frac{89}{48}\delta(\vec{\chi}_s\cdot\vec{\chi}_a), \tag{A24}$$

$$b_5 = -\frac{8191}{672}\pi - \frac{9}{2}s_l - \frac{13}{16}\delta\sigma_l + \nu\left[-\frac{583}{24}\pi + \frac{272}{9}s_l + \frac{43}{4}\delta\sigma_l\right], \tag{A25}$$

$$b_6 = \frac{6643739519}{69854400} + \frac{16}{3}\pi^2 - \frac{1712}{105}\gamma_E - \frac{856}{105}\log(16x) + \left(\frac{-134543}{7776} + \frac{41}{48}\pi^2\right)\nu - \frac{94403}{3024}\nu^2 - \frac{775}{324}\nu^3 - 16\pi s_l - \frac{31\pi}{6}\delta\sigma_l, \tag{A26}$$

$$b_7 = \left(\frac{476645}{6804} + \frac{6172}{189}\nu - \frac{2810}{27}\nu^2\right)s_l + \left(\frac{9535}{336} + \frac{1849}{126}\nu - \frac{1501}{36}\nu^2\right)\delta\sigma_l + \left(-\frac{16285}{504}\frac{214745}{1728}\nu + \frac{193385}{3024}\nu^2\right)\pi, \tag{A27}$$

$$b_8 = \left(-\frac{3485\pi}{96} + \frac{13879\pi}{72}\nu\right)s_l + \left(-\frac{7163\pi}{672} + \frac{130583\pi}{2016}\nu\right)\delta\sigma_l, \tag{A28}$$

where γ_E denotes Euler's constant.

2. Precession dynamics

The evolution of the orbital plane is governed by the frequency ϖ in Eq. (1a), which is defined in terms of two auxiliary quantities, $\gamma = m/r$ and $a_l = \vec{a}\cdot\hat{\ell}$:

$$\gamma = x\Bigg\{1 + \frac{3-\nu}{3}\,x + \frac{3\sigma_l + 5s_l}{3}\,x^{3/2} + \frac{12-65\nu}{12}\,x^2 + \left(\frac{30+8\nu}{9}s_l + 2\sigma_l\delta\right)\,x^{5/2} + \left[1+\nu\left(-\frac{2203}{2520} - \frac{41\pi^2}{192}\right) + \frac{229\nu^2}{36} + \frac{\nu^3}{81}\right]\,x^3 + \left(\frac{60-127\nu-72\nu^2}{12}\,s_l + \frac{16-61\nu-16}{6}\sigma_l\delta\right)\,x^{7/2} + x^2\left(\vec{s}_0^{\,2} - 3(\vec{s}_0\cdot\vec{\ell})^2\right)\Bigg\}, \tag{A29}$$

$$a_l = \frac{x^{\frac{7}{2}}}{m}\left\{7s_n + 3\sigma_n\delta + x\left[s_n\left(-\frac{29\nu}{3} - 10\right) + \sigma_n\delta\left(-\frac{9\nu}{2} - 6\right)\right] + x^2\left[s_n\left(\frac{52\nu^2}{9} + \frac{59\nu}{4} + \frac{3}{2}\right) + \sigma_n\delta\left(\frac{17\nu^2}{6} + \frac{73\nu}{8} + \frac{3}{2}\right)\right]\right\} - \frac{3x^4}{m}(\vec{s}_0\cdot\hat{\ell})(\vec{s}_0\cdot\hat{n}). \tag{A30}$$

Note that we have dropped the pure gauge term $-\frac{22}{3}\ln(r/r'_0)$ from γ. We now have

$$\varpi = \frac{a_l\,\gamma}{x^{3/2}}. \tag{A31}$$

The spins obey Eqs. (2) with

$$\vec{\Omega}_1 = \hat{\ell}\frac{x^{\frac{5}{2}}}{m}\left\{\frac{-3\delta+2\nu+3}{4} + x\left[\frac{10\nu-9}{16}\delta - \frac{\nu^2}{24} + \frac{5\nu}{4} + \frac{9}{16}\right] + x^2\left[\frac{-5\nu^2+156\nu-27}{32}\delta - \frac{\nu^3}{48} - \frac{105\nu^2}{32} + \frac{3\nu}{16} + \frac{27}{32}\right]\right\} + \frac{x^3}{m^3}\left[\frac{3m_1^2}{q}(\vec{\chi}_1\cdot\hat{n})\hat{n} - m_2^2\vec{\chi}_2 + 3m_2^2(\vec{\chi}_2\cdot\hat{n})\hat{n}\right]. \tag{A32}$$

The expression for $\vec{\Omega}_2$ is obtained by $\vec{\chi}_1 \leftrightarrow \vec{\chi}_2$, $m_1 \leftrightarrow m_2$, $\delta \leftrightarrow -\delta$ and $q \leftrightarrow 1/q$.

We re-expand the right-hand-side of Eq. (A31), and truncate the expansion for ϖ and $\vec{\Omega}_{1,2}$ at the same power of x *beyond the leading order*. We refer to the order of the last retained terms as the *precession PN order*. For the majority of comparisons presented in this paper, we truncate at 3.5PN; truncation at lower PN order is only used in Sec. III C. Note that spin-squared interactions imply the lack of circular orbits for generic orientations of the spins. We neglect these complications in the present work.

Appendix B: Useful quaternion formulas

We refer the reader to other sources [47, 60] for general introductions to quaternions. Here, we simply give a few formulas that are particularly important in this paper. First, we introduce some basic notation to be used for the four components of a general quaternion Q:

$$Q = (q_0, q_1, q_2, q_3) = q_0 + \vec{q}\,. \tag{B1}$$

In this notation, the quaternion conjugate is just $\bar{Q} = q_0 - \vec{q}$, and we note that the product of quaternions is given by

$$P\,Q = p_0\,q_0 - \vec{p}\cdot\vec{q} + p_0\vec{q} + q_0\vec{p} + \vec{p}\times\vec{q}\,. \tag{B2}$$

The norm of a quaternion Q is defined by $|Q|^2 = Q\,\bar{Q}$. The inverse of a quaternion is $Q^{-1} = \bar{Q}/|Q|^2$, which means that the inverse of a unit quaternion is simply its conjugate. The components of a unit quaternion $R = r_0 + \vec{r}$ satisfy $R\,\bar{R} = r_0^2 + \vec{r}\cdot\vec{r} = 1$. Unit quaternions are usually referred to as "rotors". Any rotation can be expressed as a rotor, where the rotor acts on a vector $\vec{v}$ according to the transformation law

$$\vec{v}\,' = R\,\vec{v}\,\bar{R}\,. \tag{B3}$$

The form of this expression ensures that $\vec{v}\,'$ is a pure vector; it has zero scalar part. To see this, we note that a quaternion has zero scalar part if and only if its conjugate equals its negative, which is true of the right-hand side above. We can use this fact, along with $\vec{p}\cdot\vec{q} = -\frac{1}{2}(\vec{p}\,\vec{q} + \vec{q}\,\vec{p})$ and the unit-norm property $R\,\bar{R} = 1$, to see that the right-hand side above is indeed an isometry. Finally, simple arguments using the cross product can show that such a transformation preserves orientation, and since the origin is fixed, it is therefore a simple rotation for any rotor R.

1. Exponential, logarithms, and square roots

The quaternions are closely analogous to complex numbers, except that quaternions do not commute in general. One striking example of this analogy is Euler's formula, which generalizes quite directly. If we define the exponential of a quaternion by the usual power series, we get for a unit vector $\hat{u}$

$$\exp[\theta\,\hat{u}] = \cos\theta + \hat{u}\sin\theta\ , \tag{B4}$$

which is precisely Euler's formula with i replaced by $\hat{u}$. Every rotor $R = r_0 + \vec{r}$ can be expressed in this form, so it is easy to see that the logarithm of any rotor has zero scalar part and is given by

$$\vec{\mathfrak{r}} \coloneqq \log R = \frac{\vec{r}}{|\vec{r}|}\,\arctan\frac{|\vec{r}|}{r_0}\ . \tag{B5}$$

It is useful to note that the logarithm of a rotor is parallel to the vector part of the rotor. Finding the magnitude of $\vec{r}$, of course, is just the usual square root of the sum of the squares of its components. And the arctan function is applied to real values, so we can use standard implementations of the `atan2` function to evaluate it. So we see that both the exponential and logarithm of quaternions are extremely simple and numerically robust to calculate.

These formulas can also be used to define general powers of quaternions. For the purposes of this paper, however, we only need one particular power of a quaternion: the square root. More specifically, given two unit vectors $\hat{u}$ and $\hat{w}$, we need the rotor that takes $\hat{w}$ to $\hat{u}$ by the smallest rotation possible, which is a rotation in their common plane. This rotor is given [47] by

$$R_{\hat{w}\to\hat{u}} = \sqrt{-\hat{u}\,\hat{w}} = \pm\frac{1-\hat{u}\,\hat{w}}{\sqrt{2[1-(\hat{u}\,\hat{w})_0]}}\ . \tag{B6}$$

In this expression, $\hat{u}\,\hat{w}$ represents the result of quaternion multiplication of the quaternions $\hat{u}$ and $\hat{w}$. $(\hat{u}\,\hat{w})_0$ represents the scalar part of this product, so that the square root in the denominator is acting on a real number. The sign ambiguity is generally irrelevant because of the double-sided transformation law for vectors, Eq. (B3). However, in certain special applications such as rotor interpolation, the sign must be chosen carefully to be continuous [47].

2. Deriving the frame rotor from $\hat{\ell}$ and $\hat{n}$

For both numerical relativity simulations and Post-Newtonian evolutions we have data about the positions and velocities of the black holes, that can be used to derive the frame rotor R_f, cf. Fig. 2. Given positions of the black holes as functions of time, it's a simple matter to calculate their unit separation vector $\hat{n}$, and then to calculate $\hat{\ell}$ using

$$\Omega\,\hat{\ell} = \hat{n}\times\dot{\hat{n}}\ . \tag{B7}$$

Going from $\hat{\ell}$ and $\hat{n}$ to the frame rotor R_f, the idea is to first rotate $\hat{z}$ onto $\hat{\ell}$. This will also rotate $\hat{x}$ onto some $\hat{x}'$. We then need to rotate $\hat{x}'$ onto $\hat{n}$, while leaving $\hat{\ell}$ in place. Of course, the $\hat{n}$-$\hat{x}'$ is orthogonal to $\hat{\ell}$, so we just perform a rotation in that plane. This is easily accomplished by the following formula:

$$R_i = \sqrt{-\hat{\ell}\,\hat{z}}\ , \tag{B8a}$$

$$R_\mathrm{f} = \sqrt{-\hat{n}\,(R_i\,\hat{x}\,\bar{R}_i)}\ R_i\ . \tag{B8b}$$

Again, the square roots are to be evaluated using Eq. (B6).

3. Comparing frame rotors

Reference [47] introduced a simple, geometrically invariant measure R_Δ that encodes the difference between two precessing systems as a function of time, easily reduced to a single real number Φ_Δ expressing the magnitude of that difference. These quantities were mentioned in Sec. II C without much motivation, here we briefly review that motivation.

In general, we assume that there are two (analytical or numerical) descriptions of the same physical system, and that we have two corresponding frames R_fA and R_fB. To understand the difference between the frames, we can simply take the rotation that takes one frame onto the other. In this case, the rotor taking frame A onto frame B is

$$R_\Delta \coloneqq R_\mathrm{fB}\,\bar{R}_\mathrm{fA}. \tag{B9}$$

Rotors compose by left multiplication, so it is not hard to see that this does indeed take R_fA onto R_fB because the inverse of R_fA is just its conjugate, so $R_\Delta\,R_\mathrm{fA} = R_\mathrm{fB}$.

A particularly nice feature of R_Δ is that it is completely independent of the inertial basis frame $(\hat{x},\hat{y},\hat{z})$ with respect to which we define the moving frames. That is, if we have another basis frame $(\hat{x}',\hat{y}',\hat{z}')$, there is some R_δ such that $\hat{x}' = R_\delta\,\hat{x}\,\bar{R}_\delta$, etc. The frame rotors would transform as $R_\mathrm{fA} \mapsto R'_\mathrm{fA} = R_\mathrm{fA}\,R_\delta$, in which case we obtain

$$R'_\mathrm{fB}\,\bar{R}'_\mathrm{fA} = R_\mathrm{fB}\,R_\delta\,\bar{R}_\delta\,\bar{R}_\mathrm{fA} = R_\mathrm{fB}\,\bar{R}_\mathrm{fA}. \tag{B10}$$

That is, R_Δ is invariant.

Now, we seek a relevant measure of the magnitude of the rotation R_Δ. We know that it may be written as a rotation through an angle ϕ about an axis $\hat{v}$. Clearly, ϕ is the measure we seek. The rotor corresponding to such a rotation is given by $R = \exp[\phi\,\hat{v}/2]$. Thus, to find the angle, we just use the logarithm: $\phi = 2|\log R|$, where the norm is the usual vector norm. Again, the formula for the logarithm of a rotor is a simple combination of standard trigonometric functions applied to real numbers, as

shown above. Using this interpretation with our difference rotor, we see that the appropriate definition is

$$\Phi_\Delta \coloneqq 2\left|\log\left[R_{\mathrm{fB}}\,\bar{R}_{\mathrm{fA}}\right]\right| \ . \tag{B11}$$

There is information contained in the direction of the logarithm. For example, the component along $\hat{\ell}$ is related to the difference in orbital phase for non-precessing systems, while the component orthogonal to $\hat{\ell}$ is related to the direction and magnitude of the difference in $\hat{\ell}$ itself. For the sake of simplicity, however, we focus on the magnitude of the logarithm, as given above.

4. Inadequacy of $\Phi_A - \Phi_B$ for comparisons of precessing systems

We claim that it is impossible—when analyzing precessing systems—to compare two rotations R_A and R_B in a non-degenerate and geometrically invariant way by defining some phases Φ_A and Φ_B for them separately, and then comparing them as $\Phi_A - \Phi_B$. Here, "non-degenerate" means that the phase difference is zero if and only if R_A and R_B represent the same rotation, and "geometrically invariant" means that the result is not affected by an overall rotation of the basis used to define R_A and R_B. In this section, we prove that statement.

We begin by defining a function Φ such that $\Phi(R_A) = \Phi_A$ and $\Phi(R_B) = \Phi_B$. The domain of this function is a rotation group, which could be the one-dimensional group U(1) for non-precessing systems, but must be the full three-dimensional group[8] SU(2) for general precessing systems. The range of Φ is the usual range of phases, the additive group of real numbers modulo 2π. It will be useful to note that this is isomorphic to U(1). Finally, non-degeneracy is the condition that $\Phi_A - \Phi_B = 0$ [or equivalently $\Phi(R_A) = \Phi(R_B)$] if and only if $R_A = \pm R_B$.

The condition of geometric invariance can be written as a condition on Φ itself. If, for example, we measure everything with respect to some basis $(\hat{x}, \hat{y}, \hat{z})$, and then measure again with respect to some other basis $(\hat{x}', \hat{y}', \hat{z}')$, we should get the same answer. Now, there is some rotor R_δ that takes the first basis into the second. If R_A is defined with respect to the first basis, then the equivalent quantity will be $R_A\,R_\delta$ with respect to the second. Geometric invariance is then the statement

$$\Phi(R_A\,R_\delta) - \Phi(R_B\,R_\delta) = \Phi(R_A) - \Phi(R_B), \tag{B12}$$

for *any* choice of R_δ in SU(2). We will show that there is no such Φ because the rotation group SU(2) is not isomorphic to U(1).

Since Eq. (B12) is true for *any* rotor R_δ, we can choose $R_\delta = R_B^{-1}$, and find that

$$\Phi(R_A\,R_B^{-1}) - \Phi(1) = \Phi(R_A) - \Phi(R_B). \tag{B13}$$

Now, we define another function $\Phi'(R) = \Phi(R) - \Phi(1)$. The last equation becomes

$$\Phi'(R_A\,R_B^{-1}) = \Phi'(R_A) - \Phi'(R_B). \tag{B14}$$

In exactly the same way, we can see that

$$\Phi'(R_B\,R_A^{-1}) = \Phi'(R_B) - \Phi'(R_A) = -\Phi'(R_A\,R_B^{-1}). \tag{B15}$$

This must be true for *all* values of R_A and R_B, so we have shown that

$$\Phi'(R^{-1}) = -\Phi'(R), \tag{B16}$$

for arbitrary R. Therefore, we can also see from Eq. (B14) that

$$\Phi'(R_1\,R_2) = \Phi'(R_1) + \Phi'(R_2), \tag{B17}$$

for arbitrary R_1 and R_2. This is precisely the statement that Φ' is a homomorphism [from SU(2) to the additive group of real numbers modulo 2π].

However, now we can impose the condition that $\Phi_A - \Phi_B = 0$ if and only if $R_A = \pm R_B$. Using the properties of homomorphism, it is clear that this is equivalent to the statement that the set of all elements that map to 0 under Φ' is $\ker\Phi' = \{-1, 1\}$. Then, the First Group Isomorphism Theorem [61] says that the image of Φ' is isomorphic to SU(2) modulo this kernel, which of course is just SO(3). But the image of Φ' is (possibly a subgroup of) the group U(1), which is obviously not isomorphic to SO(3).[9] Therefore, it is impossible to construct a function fulfilling our requirements for precessing systems.

It is, however, interesting to note that if our rotation group were not SU(2), but the one-dimensional rotation group U(1), there would be no contradiction. This is how it *is* possible to construct a useful measure of the form $\Phi_A - \Phi_B$ for *non*-precessing systems, because the rotations can be restricted to rotations about the orbital axis. On the other hand, for precessing systems, the measure Φ_Δ described in Secs. II C and B 3 is able to satisfy both key features of a useful measure (non-degeneracy and geometric invariance) because it simply does not attempt to define a homomorphism from the rotation group; rather, it defines a (non-homomorphic but invariant and non-degenerate) function from *two copies of* the rotation group onto phases, $\mathrm{SU}(2) \times \mathrm{SU}(2) \to \mathrm{U}(1)$.

---

[8] Even though it is a double cover of the physical rotation group SO(3), we use SU(2) here for consistency of notation, because it is the group of unit quaternions. The proof would actually be slightly simpler for SO(3); we would have $\Phi(R_A) = \Phi(R_B)$, if and only if $R_A = R_B$, and $\ker\Phi' = \{1\}$.

[9] This statement will not be controversial, but for form's sake we can prove it simply by noting that U(1) is commutative, whereas we can find elements of SO(3) that do not commute.

[1] The LIGO Scientific Collaboration, (2014), arXiv:1411.4547 [gr-qc].
[2] T. Accadia, F. Acernese, F. Antonucci, P. Astone, G. Ballardin, *et al.*, Class.Quant.Grav. **28**, 114002 (2011).
[3] B. Abbott *et al.* (LIGO Scientific Collaboration), Rept. Prog. Phys. **72**, 076901 (2009), arXiv:0711.3041 [gr-qc].
[4] T. A. Apostolatos, C. Cutler, G. J. Sussman, and K. S. Thorne, Phys. Rev. D **49**, 6274 (1994).
[5] L. Pekowsky, R. O'Shaughnessy, J. Healy, and D. Shoemaker, Phys. Rev. D **88**, 024040 (2013), arXiv:1304.3176 [gr-qc].
[6] M. Boyle, L. E. Kidder, S. Ossokine, and H. P. Pfeiffer, "Gravitational-wave modes from precessing black-hole binaries," (2014), arXiv:1409.4431 [gr-qc].
[7] L. Blanchet, Living Reviews in Relativity **17** (2014), 10.12942/lrr-2014-2.
[8] F. Ohme, Class.Quant.Grav. **29**, 124002 (2012), arXiv:1111.3737 [gr-qc].
[9] T. Damour, A. Nagar, and M. Trias, Phys. Rev. D **83**, 024006 (2011), arXiv:1009.5998 [gr-qc].
[10] M. Boyle, Phys. Rev. D **84**, 064013 (2011).
[11] F. Ohme, M. Hannam, and S. Husa, Phys. Rev. D **84**, 064029 (2011).
[12] I. MacDonald, S. Nissanke, and H. P. Pfeiffer, Class. Quantum Grav. **28**, 134002 (2011), arXiv:1102.5128 [gr-qc].
[13] I. MacDonald, A. H. Mroué, H. P. Pfeiffer, M. Boyle, L. E. Kidder, M. A. Scheel, B. Szilágyi, and N. W. Taylor, Phys. Rev. D **87**, 024009 (2013), arXiv:1210.3007 [gr-qc].
[14] A. H. Nitz, A. Lundgren, D. A. Brown, E. Ochsner, D. Keppel, *et al.*, Phys.Rev. **D88**, 124039 (2013), arXiv:1307.1757 [gr-qc].
[15] M. Hannam, P. Schmidt, A. Bohé, L. Haegel, S. Husa, *et al.*, Phys.Rev.Lett. **113**, 151101 (2014), arXiv:1308.3271 [gr-qc].
[16] A. Taracchini, A. Buonanno, Y. Pan, T. Hinderer, M. Boyle, *et al.*, Phys.Rev. **D89**, 061502 (2014), arXiv:1311.2544 [gr-qc].
[17] Y. Pan, A. Buonanno, A. Taracchini, L. E. Kidder, A. H. Mroué, *et al.*, Phys.Rev. **D89**, 084006 (2014), arXiv:1307.6232 [gr-qc].
[18] A. H. Mroué, M. A. Scheel, B. Szilágyi, H. P. Pfeiffer, M. Boyle, D. A. Hemberger, L. E. Kidder, G. Lovelace, S. Ossokine, N. W. Taylor, A. i. e. i. f. Zenginoğlu, L. T. Buchman, T. Chu, E. Foley, M. Giesler, R. Owen, and S. A. Teukolsky, Phys. Rev. Lett. **111**, 241104 (2013).
[19] B. M. Barker and R. F. O'Connell, Phys. Rev. **D12**, 329 (1975).
[20] L. E. Kidder, C. M. Will, and A. G. Wiseman, Phys. Rev. D **47**, 3281 (1993).
[21] L. E. Kidder, Phys. Rev. **D52**, 821 (1995), arXiv:gr-qc/9506022.
[22] S. Marsat, A. Bohe, L. Blanchet, and A. Buonanno, (2013), arXiv:1307.6793 [gr-qc].
[23] A. Boh, G. Faye, S. Marsat, and E. K. Porter, (2015), arXiv:1501.01529 [gr-qc].
[24] A. Bohé, S. Marsat, G. Faye, and L. Blanchet, Class. Quantum Grav. **30**, 075017 (2013).
[25] J. Hartung and J. Steinhoff, Annalen Phys. **523**, 919 (2011), arXiv:1107.4294 [gr-qc].
[26] R. A. Porto and I. Z. Rothstein, Phys.Rev. **D78**, 044013 (2008), arXiv:0804.0260 [gr-qc].
[27] M. Levi and J. Steinhoff, JCAP **1412**, 003 (2014), arXiv:1408.5762 [gr-qc].
[28] S. Marsat, (2014), arXiv:1411.4118 [gr-qc].
[29] M. Levi and J. Steinhoff, (2014), arXiv:1410.2601 [gr-qc].
[30] T. Damour, B. R. Iyer, and B. S. Sathyaprakash, Phys. Rev. D **63**, 044023 (2001), gr-qc/0010009.
[31] P. Ajith, Phys.Rev. **D84**, 084037 (2011), arXiv:1107.1267 [gr-qc].
[32] M. Boyle, D. A. Brown, L. E. Kidder, A. H. Mroué, H. P. Pfeiffer, M. A. Scheel, G. B. Cook, and S. A. Teukolsky, Phys. Rev. D **76**, 124038 (2007).
[33] L. Santamaría, F. Ohme, P. Ajith, B. Brügmann, N. Dorband, M. Hannam, S. Husa, P. Mösta, D. Pollney, C. Reisswig, E. L. Robinson, J. Seiler, and B. Krishnan, Phys. Rev. D **82**, 064016 (2010), arXiv:1005.3306 [gr-qc].
[34] L. T. Buchman, H. P. Pfeiffer, M. A. Scheel, and B. Szilagyi, Phys. Rev. D **86**, 084033 (2012), arXiv:1206.3015 [gr-qc].
[35] H. Friedrich, Commun. Math. Phys. **100**, 525 (1985).
[36] D. Garfinkle, Phys. Rev. D **65**, 044029 (2002).
[37] F. Pretorius, Class. Quantum Grav. **22**, 425 (2005).
[38] L. Lindblom, M. A. Scheel, L. E. Kidder, R. Owen, and O. Rinne, Class. Quantum Grav. **23**, S447 (2006).
[39] M. A. Scheel, M. Boyle, T. Chu, L. E. Kidder, K. D. Matthews and H. P. Pfeiffer, Phys. Rev. D **79**, 024003 (2009), arXiv:gr-qc/0810.1767.
[40] T. Chu, H. P. Pfeiffer, and M. A. Scheel, Phys. Rev. D **80**, 124051 (2009), arXiv:0909.1313 [gr-qc].
[41] L. Lindblom and B. Szilágyi, Phys. Rev. D **80**, 084019 (2009), arXiv:0904.4873.
[42] B. Szilagyi, L. Lindblom, and M. A. Scheel, Phys. Rev. D **80**, 124010 (2009), arXiv:0909.3557 [gr-qc].
[43] M. W. Choptuik and F. Pretorius, Phys.Rev.Lett. **104**, 111101 (2010), arXiv:0908.1780 [gr-qc].
[44] B. Szilágyi, Int. J. Mod. Phys. D **23**, 1430014 (2014).
[45] M. A. Scheel, M. Giesler, D. A. Hemberger, G. Lovelace, K. Kuper, *et al.*, (2014), arXiv:1412.1803 [gr-qc].
[46] A. Buonanno, G. B. Cook, and F. Pretorius, Phys. Rev. D **75**, 124018 (2007), arXiv:gr-qc/0610122 [gr-qc].
[47] M. Boyle, Phys. Rev. D **87**, 104006 (2013).
[48] D. Kraft, Deutsche Forschungs- und Versuchsanstalt fr Luft- und Raumfahrt **88** (1988).
[49] R. E. Perez, P. W. Jansen, and J. R. R. A. Martins, Structures and Multidisciplinary Optimization **45**, 101 (2012).
[50] L. D. Paarmann, *Design and analysis of analog filters a signal processing perspective* (Kluwer Academic Publishers, Boston, 2001).
[51] J. Veitch, V. Raymond, B. Farr, W. M. Farr, P. Graff, *et al.*, (2014), arXiv:1409.7215 [gr-qc].
[52] M. Hannam, S. Husa, F. Ohme, D. Müller, and B. Brügmann, Phys. Rev. D **82**, 124008 (2010), arXiv:1007.4789.
[53] G. Lovelace, R. Owen, H. P. Pfeiffer, and T. Chu, Phys. Rev. D **78**, 084017 (2008).
[54] R. Owen, *Topics in Numerical Relativity: The periodic standing-wave approximation, the stability of constraints*

in free evolution, and the spin of dynamical black holes, Ph.D. thesis, California Institute of Technology (2007).
[55] G. B. Cook and B. F. Whiting, Phys. Rev. D **76**, 041501(R) (2007).
[56] K. G. Arun, A. Buonanno, G. Faye, and E. Ochsner, Phys. Rev. D **79**, 104023 (2009), arXiv:0810.5336 [gr-qc].
[57] M. Hannam, S. Husa, F. Ohme, and P. Ajith, Phys. Rev. D **82**, 124052 (2010), arXiv:1008.2961 [gr-qc].
[58] http://www.black-holes.org/SpEC.html.
[59] C. Loken, D. Gruner, L. Groer, R. Peltier, N. Bunn, M. Craig, T. Henriques, J. Dempsey, C.-H. Yu, J. Chen, L. J. Dursi, J. Chong, S. Northrup, J. Pinto, N. Knecht, and R. V. Zon, J. Phys.: Conf. Ser. **256**, 012026 (2010).
[60] C. Doran and A. Lasenby, *Geometric algebra for physicists*, 3rd ed. (Cambridge University Press, 2003).
[61] D. S. Dummit and R. M. Foote, *Abstract algebra*, 2nd ed. (Prentice Hall, Hoboken, NJ, 1999).